Nuclear Inst. and Methods in Physics Research, A 970 (2020) 163373

Contents lists available at ScienceDirect

Nuclear Inst. and Methods in Physics Research, A

journal homepage: www.elsevier.com/locate/nima

Position-sensitive vacuum photon detectors

Thierry Gys *, Christian Joram

CERN, EP Department, CH-1211 Geneva 23, Switzerland

ARTICLE INFO

Keywords:
Cherenkov light imaging
High-energy physics
Photo-conversion
Multi-anode photomultiplier tubes
Micro-channel plates
Hybrid photon detectors

ABSTRACT

This article reviews the principles, performance and limitations of position-sensitive vacuum photon detectors which find applications in high-energy physics experiments. Particular emphasis is devoted to multi-anode photo-multiplier tubes, devices based on micro-channel plates and hybrid photon detectors. Over the past 25 years, innovation in industrial environments, research centres and universities has led to the invention and consequent optimization of a number of position-sensitive photon detectors. Miniaturization of known principles and components or the smart combination of established concepts allowed to build new classes of finely-segmented photodetectors which in turn enabled new applications in high-energy physics, but also elsewhere. The imaging of Cherenkov light in hostile hadron environments like at the CERN Large Hadron Collider is perhaps one of the most demanding applications which would not have been possible without this breakthrough.

1. Introduction

Today, 42 years after the pioneering work by Tom Ypsilantis and Jacques Séguinot [1], the precise and efficient imaging of Cherenkov photons remains challenging, particularly in high rate and high occupancy environments like for instance at modern hadron colliders.

The separation of particle species through the combined measurement of their Cherenkov angles θ (equivalent to their relativistic speed β) and their momenta relies on the precise localization of a sufficient number of Cherenkov photons within a short time interval and with little background.

This is generally true for classical RICH (Ring Imaging CHerenkov) geometries [5] as well as for DIRC (Detection [of] Internally Reflected Cherenkov [light]) [6]. The properties of the photodetector have a crucial impact on several contributions to the Cherenkov angle resolution:

- The segmentation of the readout plane of a Cherenkov detector drives the pixel error. Millimetre-size elements can increase the number of readout channels towards hundreds of thousand. Compared to individual mono-channel photodetectors, multi-pixel devices with an adequate form factor can reduce cost and facilitate readout, voltage biasing and mechanical integration.
- The photodetector shall have large active-area coverage, without significant inter-pixel or peripheral dead zones.
- The sensitivity range, from the threshold of the photosensitive material to the cut-off of the entrance window, and the quantum efficiency distribution, impact on the number of detected photoelectrons, but also influence the chromatic error due to the optical dispersion of the radiator medium.
- As the Cherenkov effect is a weak light source, at least for minimum ionizing particles, photodetectors have to be capable of efficiently detecting individual photons. At the same time, the detector shall not suffer from excessive dark or other noise (at the single photoelectron level) which pollutes the data and complicates Cherenkov ring finding.

In addition, other characteristics like tolerance to magnetic fields and ionizing radiation, gain uniformity, longevity and cost may be decisive.

In other applications, such as calorimetry or scintillating fibre tracking, where the same or similar multi-pixel photodetectors are being used, signal linearity and gain uniformity over the tube surface may be key requirements.

This review deals with position-sensitive vacuum photon detectors. Over the past 15–20 years they have been the preferred solution for covering the large focal planes of the second-generation Cherenkov detectors (like HERA-B, LHCb, COMPASS, etc.) with finely-segmented and single-photon sensitive devices.

During the same period, multi-pixel Geiger-mode avalanche photodiodes, now commonly called Silicon Photo-Multipliers (SiPM), evolved from small laboratory samples, with relatively low sensitivity, high dark noise and some other unwanted features, to a mature, robust and cost-effective single-photon sensitive detector. They are about to replace vacuum photo-tubes in many domains such as scintillating

* Corresponding author.
E-mail addresses: Thierry.Gys@cern.ch (T. Gys), Christian.Joram@cern.ch (C. Joram).

https://doi.org/10.1016/j.nima.2019.163373
Received 29 October 2019; Received in revised form 19 December 2019; Accepted 27 December 2019
Available online 7 January 2020

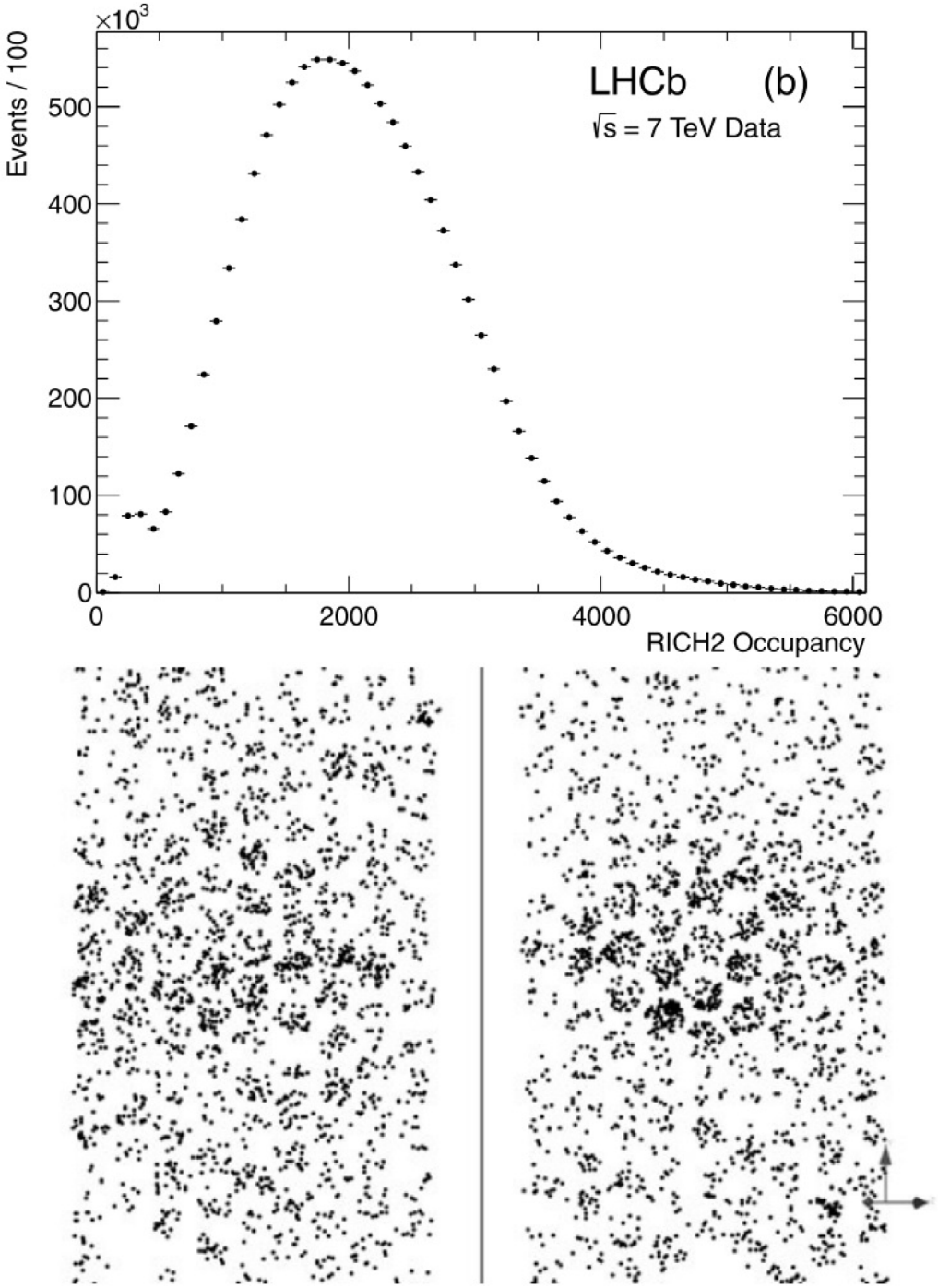

Fig. 1. Distribution of the number of pixel hits per event in the RICH 2 of LHCb. An example of a typical LHCb event as seen on the two detection planes (710 × 1477 mm^2 each) of RICH 2 is shown below the distribution [2].

fibre tracking [7], calorimetry [8], medical [9] and industrial (automotive) [10] applications. However, in domains where lowest dark noise and operation in harsh radiation fields are required such as Cherenkov imaging at hadron accelerators like the CERN Large Hadron Collider (LHC), vacuum photodetectors are still the preferred choice. Conversely, the rate of radiation-induced dark noise in SiPMs can be reduced by lowering the operational temperature — exponentially by a factor two every 8 K. This method, even if technically demanding, may in the medium-term future pave the way for the use of SiPMs also in these domains.

To set the scene, Fig. 1 gives an impression of the typical challenge [2]. In the RICH 2 detector of the LHCb experiment [11], Cherenkov photons are detected by 288 hybrid photon detectors with 1024 pixels each, instrumenting the two focal planes (see Section 5). As the upper plot shows, the average hit multiplicity is about 2000 with tails in excess of 5000 hit pixels. The lower part shows the chart of the photon hits for a single proton–proton collision in the LHC. Thanks to the fine segmentation of the photodetectors, the occupancy per pixel remains below 1%.

In this article, Section 2 introduces the basic principles of photo-conversion in vacuum photo-cathodes. Sections 3–5 cover the technologies and applications in Cherenkov light imaging of Multi-Anode Photo-Multiplier Tubes (MAPMTs), Micro-Channel Plate Photo-Multiplier

Tubes (MCP-PMTs) and Hybrid Photon Detectors (HPDs), respectively. The article is completed by a summary and an outlook in Section 6.

2. Photo-conversion in vacuum photo-cathodes

This section is a brief reminder of basic principles and limitations of photo-cathodes used in vacuum tubes. Practically all position-sensitive vacuum photodetectors make use of a very thin transmission-mode photo-cathode layer deposited in a multi-step vacuum evaporation process (Physical Vapour Deposition) onto the inner surface of the tube's entrance window. Photoemission is usually described as a three-step process, schematically shown in the band model in Fig. 2: (1) photon absorption and energy transfer to an electron, (2) diffusion (random walk) with gradual loss of energy and (3) escape from the surface into the tube vacuum. The photo-cathode thickness, typically a few tens of nm, is crucial in order to find the best compromise between maximum light absorption on the one hand and photoelectron escape probability on the other. The ratio of the numbers of escaping electrons to incident photons is referred to as Quantum Efficiency QE.

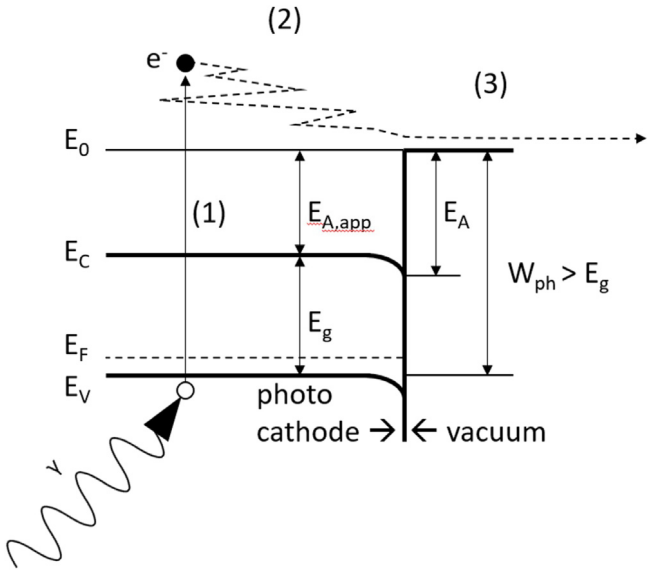

Fig. 2. Simplified representation of photo-conversion in a semiconductor (after [3]). A photon needs the minimum energy $E_g + E_{A,app}$ to release an electron into the vacuum (energy level E_0). The apparent electron affinity $E_{A,app}$ is reduced as a consequence of the deformation of the valence and conduction bands close to the surface, an effect which can be enhanced by the adsorption of alkali metals (mainly Caesium).

Pressure and quality of the vacuum, temperature and cleanliness of the substrate, purity of the evaporated materials, evaporation rates and quantities — they all have an impact on the quality of the photo-cathode. Most of the photo-tubes intended for the visible and near-UV range are of the bi-alkali (K_2CsSb) and multi-alkali (Na_2KCsSb) type. While fundamental information can be found for example in the classic book by Sommer [12], the handful of companies world-wide fabricating photo-tubes keep the details of the processes and recipes confidential and only few research groups [13,14] have embarked on the adventure of producing sealed photo-tubes.

Standard photomultiplier tubes are generally produced with an internal process, in which the interior of the completely assembled photo-tube is evacuated through a small glass pumping stud which can be sealed off by a flame at the end of the process. The set-up is placed inside an oven for temperature control during bake-out and processing. The photo-cathode is generated by controlled heating (Joule effect) of small Sb and alkali sources (in the form of special dispensers) also included in the tube. Several tubes can be processed in parallel.

Special tubes, including hybrid tubes, MCP-tubes and multi-anode tubes are usually processed in technically more demanding external or transfer processes. The cathode and anode parts of the tube are physically separated during photo-cathode processing in order to avoid uncontrolled pollution of e.g. Si sensors or MCPs with alkali metals. Vacuum sealing needs to be accomplished in-situ, which is a challenge particularly in view of the required stability over many years. Also combinations of external and internal processes exist where, prior to tube assembly, a thin Sb layer is deposited on the inside of the entrance window. The tube is then assembled, sealed and evacuated via a special pumping stud like in an internal process. The Sb layer is activated by

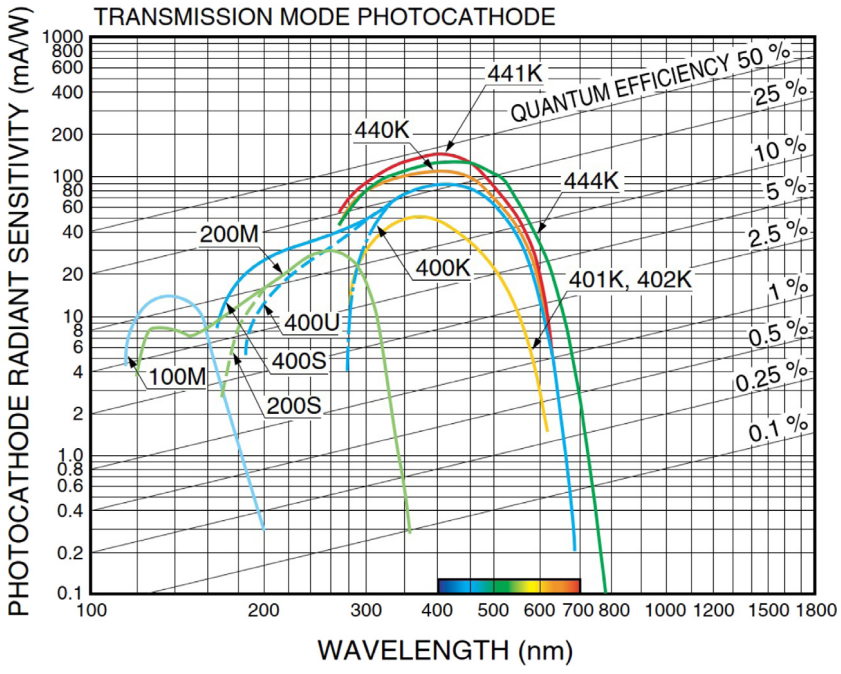

Fig. 3. Typical spectral response of photo-cathodes [4]. The figure shows the radiant sensitivity S in mA/W. The oblique lines represent quantum efficiency $QE = S \cdot 1240/\lambda$. Note the logarithmic scale of both axes.

the alkali metals and the tube is finally sealed off. This latter process appears to be the method used by Hamamatsu[1] for the fabrication of their MAPMT series [15].

Fig. 3 shows the typical radiant sensitivity S versus wavelength (both in logarithmic scale) for various photo-cathode types. In this plot the diagonal lines representing quantum efficiency $QE = S \cdot 1240/\lambda$ are straight. It should be noted that, by convention, the quantum efficiency of a photo-tube includes the transparency of the entrance window, however not the probability to collect, multiply and detect the photoelectron. While for several decades the best (bi-alkali) photo-cathodes (marked as 400 K in Fig. 3) peaked around 400 nm at about $QE = 25\%$, several producers achieve now higher quantum efficiencies. The so-called super (440 K) and ultra bi-alkali (441 K) cathodes of HPK achieve QE values of up to about 45% without losing spectral coverage. The process changes which led to this important progress, directly impacting on the performance of a Cherenkov detector, are kept confidential by the company.

3. Multi-anode PMTs

Conventional miniaturization of PMTs based on glass bodies and discrete dynode assemblies is challenging. Several producers manage to fabricate head-on tubes of about 1 cm diameter,[2] with typically 80% active area. Apart from cost and integration complexity, which are prohibitive for large-scale applications, also the active-area fraction, even in an ideal hexagonally closed-packed arrangement[3] remains at a modest 58%.

3.1. Principle, designs and construction

The successful approach to position sensitivity is based on the parallel (side-by-side) arrangement of several dynode channels and anodes in the same tube. The first dynodes form a layer parallel to, and at mm-distance, from the photo-cathode. This so-called proximity focusing electron-optical design of such a multi-anode PMT has to ensure the efficient and undistorted transfer of the electrons released from the photo-cathode to the first dynode. The subsequent steps of the dynode structure need to limit the lateral spreading of the growing electron cloud and prevent electrons from entering into adjacent channels, which contributes to unwanted cross-talk. Fig. 4 gives an overview of dynode types used in position-sensitive PMTs.

A technically simple solution is to use stacks of crossed fine-wire meshes as dynodes. The suitability of proximity focusing to achieve position sensitivity in a PMT was demonstrated by Kume et al. [16] in 1985. One year later, a team led by the same author presented the first 3 inch position-sensitive PMT based on a 11-stage mesh dynode system [17]. The anode consisted of two crossed-wire grids (x and y) with 4 mm pitch, a technology which did not yet allow for true multi-anode readout. The collected charges Q were divided by two resistor chains at the ends of the grids. The coordinates x and y could then be reconstructed according to the centroid formulae, e.g. $x = Q_{x,1}/(Q_{x,1} + Q_{x,2})$. The intrinsic spatial spread of the charge cloud was found to be 4.3 mm (FWHM), with contributions of 1.5 mm from the photo-cathode to the first dynode and 4 mm due to the spread in the dynode structure itself (Dy1–Dy11). Even though this PMT featured special suppressor grids on top of every mesh layer, the relatively large spread at the anode level shows the limitation of the conventional mesh technology.

A breakthrough was the invention of the metal channel dynode technology and the very compact metal can package [18] in the early 1990s, demonstrated shortly after in crossed-wire position sensitive

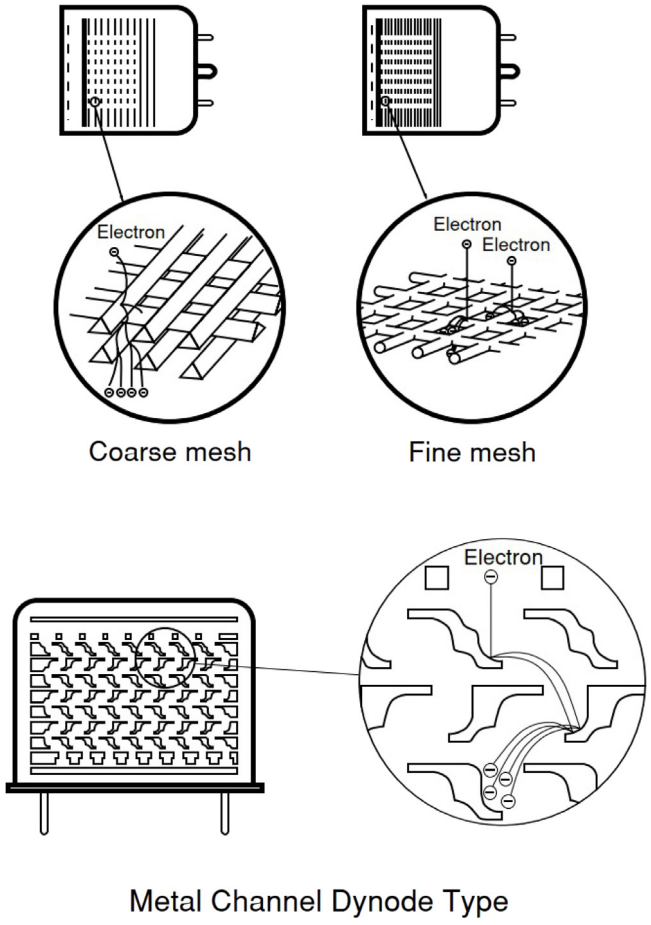

Fig. 4. Schematic of dynode types used in position-sensitive PMTs [4].

tubes (R7600 series) with square-shaped metal cans [19,20]. The metal channel dynodes were made from precisely micro-machined sheets with complex openings whose geometry was the result of electron-optical simulations and key to efficient collection at the first dynode, good single photon sensitivity and low inter-channel cross-talk of about 1%. The metal can technology allowed to build square tubes of roughly 1 square-inch size with reasonable active area coverage, initially 43%, significantly improved in later models. The R5900 family [21] with true multi-anode readout was introduced in 1997 featuring anode segmentation into 4, 16 or 64 readout pads. Soon after followed the so-called flat panel PMT (52 × 52 mm^2) [22], providing a 4 times larger area at only 12 mm height and an active-area fraction close to 90%. Over the years HPK continuously improved the design and performance of the various MAPMT types. Certain tubes were customized for detectors requiring a large quantity. This has led to a multitude of tube types and names.

In the 1990s also Philips pursued a similar development which led to the XP1700 family [23] with a stack of circular-structure metal foil dynodes and a 64 or 96-fold segmented 10th dynode with 2.54 mm spacing. The large round package (D ≈ 65 mm) led to a low active-area fraction which made the tube unsuitable for Cherenkov Imaging applications. The tube was actually targeting applications in scintillating fibre detectors.

Table 1 gives an overview of the characteristics of some MAPMT types, produced by HPK and Philips. Representative of the modern MAPMT generation, the relevant performance and limitations [24] of the H12700 flat panel with 64 channels of 6 × 6 mm^2 size (see Fig. 5) are also briefly summarized. The device provides high QE (33 %) and charge gain of a few 10^6, with a spread across the 64 pixels

[1] Hamamatsu Photonics K.K., Japan; in the following abbreviated as HPK.

[2] E.g. HPK R1635, ET Enterprises 12B01H and HZC Photonics XP1302.

[3] A hexagonally closed-packed arrangement of round tubes with active diameter D_{act} mounted at a centre-to-centre distance of D_{c2c} results in a packing fraction $\rho = \pi D_{act}^2/(2\sqrt{3}D_{c2c}^2)$.

Table 1
Overview of MAPMT photodetectors (all from HPK except XP1702 which was produced by Philips).

MAPMT type	R5900	R7600	H8500	H12700	XP1702
overall size (mm)	27.7 □	25.7 □	52 □	52 □	≈ 65○
active size (mm)	18.1 □	18.1 □	49 □	48.5 □	25.4 □
active area fraction (%)	43	50	89	87	≈ 19
QE max. (%)	≈20	≈20	≈27	≈33	≈21

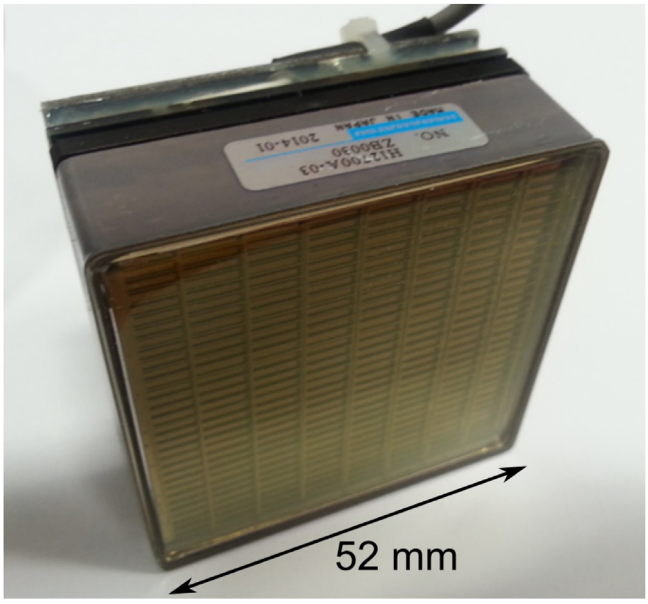

Fig. 5. Photograph of a H12700 MAPMT.
Source: Taken from [24].

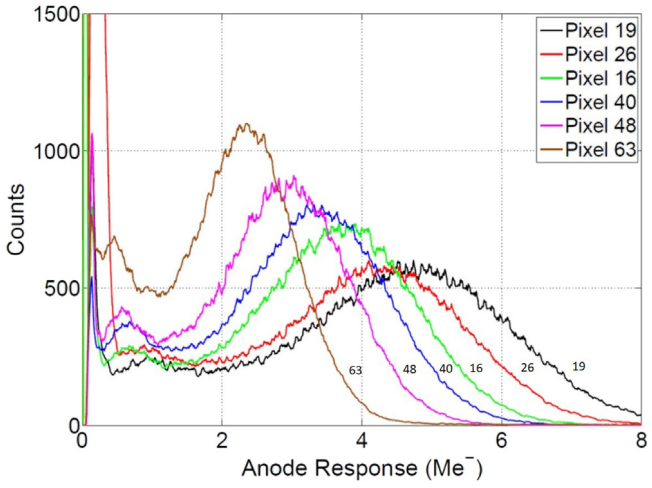

Fig. 6. Single-photoelectron pulse height distributions of a few pixels of the H12700 MAPMT. Pixels 19 and 63 are the ones with the highest and lowest gains of this tube.
Source: Taken from [24].

of a factor 2–3. This is attributed to small geometrical imperfections (manufacturing tolerances) of the dynode structure. Thanks to their compact design, they have sub-ns rise time and Transit Time Spread (TTS). As shown in Fig. 6, their pulse-height distribution achieved allows for efficient single photon detection. The dark count rate is very low ($\lesssim$ 40 Hz/cm^2 at a threshold of 10^6 e). The signal cross-talk to neighbouring channels has several origins, is directional and, in the worst case, was found to be limited to 7% of the amplitude generated by a single photon. Exposure to magnetic fields, in particular when aligned with the tube axis, leads to a pronounced reduction (about −20% at 2.5 mT) of the collection efficiency at the first dynode. For fields up to 2.5 mT, a thin local μ-metal or similar layer recovers the full efficiency. The gain varies also slightly with ambient temperature. In the range from 10 to 50 °C a slope of −0.25%/K has been found. Operation of the tube for 3000 h under light exposure, very close to the maximum anode current rating of 100 μA, revealed gain variations of $|\Delta G| \leq 20\%$. In the latter two cases the gain can be re-adjusted by adapting the bias voltage.

3.2. Applications in Cherenkov imaging

As discussed in Section 1 the main requirements for the photon detector in Cherenkov imaging applications are mm-scale segmentation, high QE in the visible and near-UV range and good single-photon sensitivity. A high active-area fraction is also crucial as it directly determines the number of detected photons. The above-described multi-anode PMTs fulfil these requirements, except for the active-area fraction which was in the first versions still below 50%. Lens solutions were developed which demagnified the image corresponding to the full photodetector area to its active area. In the following a number of major Cherenkov imaging applications are described in chronological order.

3.2.1. The HERA-B RICH

The HERA-B experiment was a fixed target forward spectrometer at the DESY HERA storage ring. Designed to measure CP violation parameters in the B-sector, it included a mirror-focused RICH detector with a 2.75 m long C_4F_{10} gas radiator to separate pions from kaons up to 60 GeV/c. The B-mesons were produced in collisions of the 920 GeV halo protons with an internal wire target. The expected high interaction rates of up to 40 MHz translated to peak photon rates of

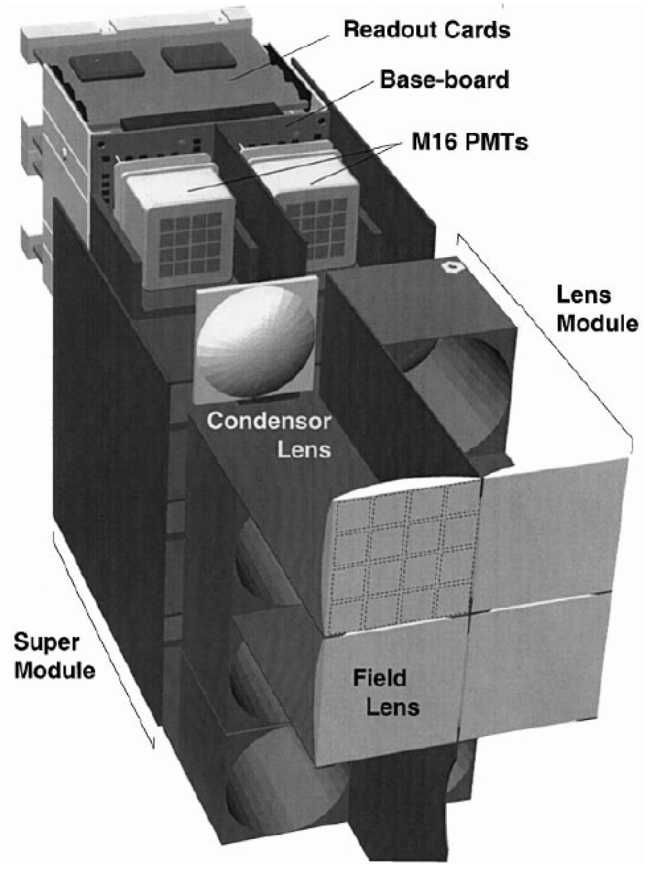

Fig. 7. Photodetector assembly with demagnifying telescope of the HERA-B RICH [25].

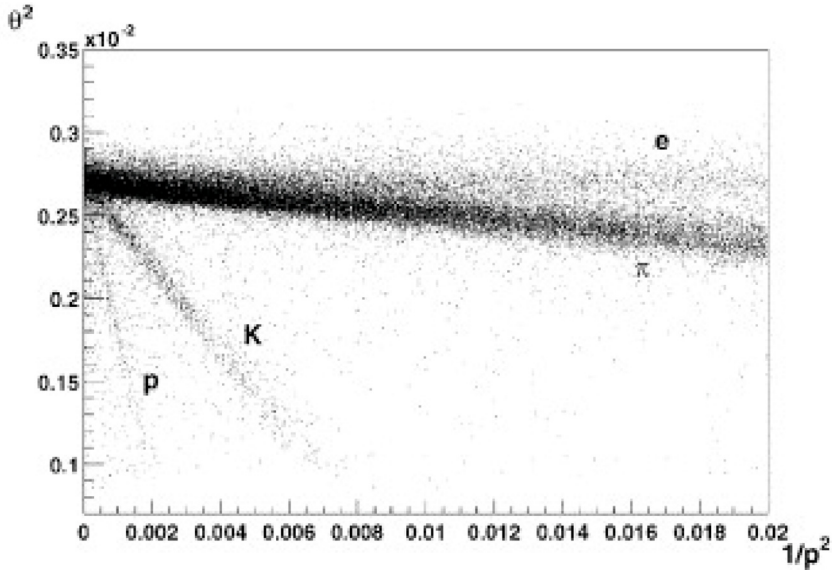

Fig. 8. Performance of the HERA-B RICH. In the plot of θ_C^2 versus $1/p^2$ the different particle species follow straight lines [25].

3 MHz/cm^2 [25]. The originally envisaged photosensitive gas chamber technology, based on the admixture of TMAE[4] vapour to the counting gas [26] and which had proved successful in the RICH detectors of the DELPHI, CRID and OMEGA experiments, had soon to be abandoned because of severe ageing phenomena [27]. Instead, it was proven that MAPMTs of the HPK R5900 series could fulfil the requirements and sustain the high photon rates [28,29]. Mounted with a pitch of 36 mm, a total of 750 MAPMTs of R5900-M4 and 1500 R5900-M16 populated the outer and inner zones of the two focal planes with a total photo-detection area of 2.9 m^2.

A two-lens telescope with a demagnification of 2:1 (= a factor of 4 in area!) was mounted in front of each MAPMT (see Fig. 7). The lenses, made from UV plastic, mapped a 36 × 36 mm^2 area on the active zone of the MAPMT, at the expense of increasing the effective pixel size at the focal plane from 4.5 mm to 9 mm (M16 tubes) and to 18 mm (M4 tubes). In the inner region, the effective pixel size error (0.46 mrad) is only modestly larger than the irreducible chromatic error (0.33 mrad) due to the dispersion of the radiator gas [30]. The efficiency of the telescope was found to be 65% with losses due to reflection (15%), absorption (15%) and geometry (5%). The number of detected photoelectrons for $\beta = 1$ particles was about 35. Fig. 8 shows the capability of this detector to identify the different particle species. In conclusion, HERA-B RICH, even though operated only from 2000 to 2003, pioneered the use of multi-anode PMTs in Cherenkov detectors, demonstrated its high-rate and low-ageing potential and therefore paved the way for several other Cherenkov imaging applications.

3.2.2. The COMPASS fast RICH

The RICH-1 of the COMPASS experiment, based on a 3 m-long mirror-focused C_4F_{10} gas radiator is in operation since 2002 [31]. Originally, its 5.5 m^2 large focal planes were instrumented with eight multi-wire proportional chambers (MWPC) featuring solid CsI photocathodes, which were vacuum-evaporated on the segmented (8 × 8 mm^2) cathode planes of the chambers. To limit ageing and instabilities of the chambers, they were operated in the COMPASS RICH at a gain of $5 \cdot 10^4$ compromising the single photoelectron detection efficiency [32]. The chambers were read out by electronics with long integration time (0.5–1.0 μs) to compensate for the reduced gain. An additional baseline restoration time of 3.5 μs led to reduced performance in the forward region where large uncorrelated background (halo of SPS muon beam) is present.

[4] Tetrakis Dimethylamino Methylene.

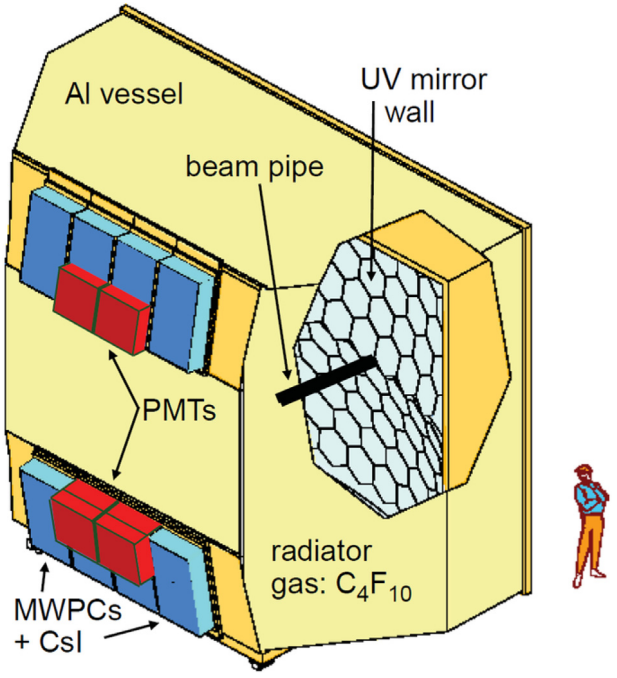

Fig. 9. Schematic view of the COMPASS RICH. In the central part of the upper and lower focal planes the MWPC + CsI photodetectors were replaced by MAPMTs with lens telescopes [32].

To overcome these rate and efficiency limitations in the central part of the focal plane, the MWPCs were replaced by 576 MAPMTs of type R7600-03-M16 with fast readout electronics [35] (see Fig. 9). Similar to HERA-B, a two-lens telescope concentrates the light by a factor 2.7. Unlike HERA-B, the lenses were made from fused silica and featured anti-reflection coating. This effort was rewarded by a high number of detected photoelectrons of 56 (for β=1, ring fully contained on MAPMT region).

It is worth mentioning that the COMPASS collaboration has recently performed another photodetector upgrade [36]. In the region above and below the MAPMTs, four new hybrid Thick-GEM/MicroMegas chambers with a total active surface of 1.5 m^2 were installed replacing the CsI MWPCs. The new technology overcomes the instabilities of the

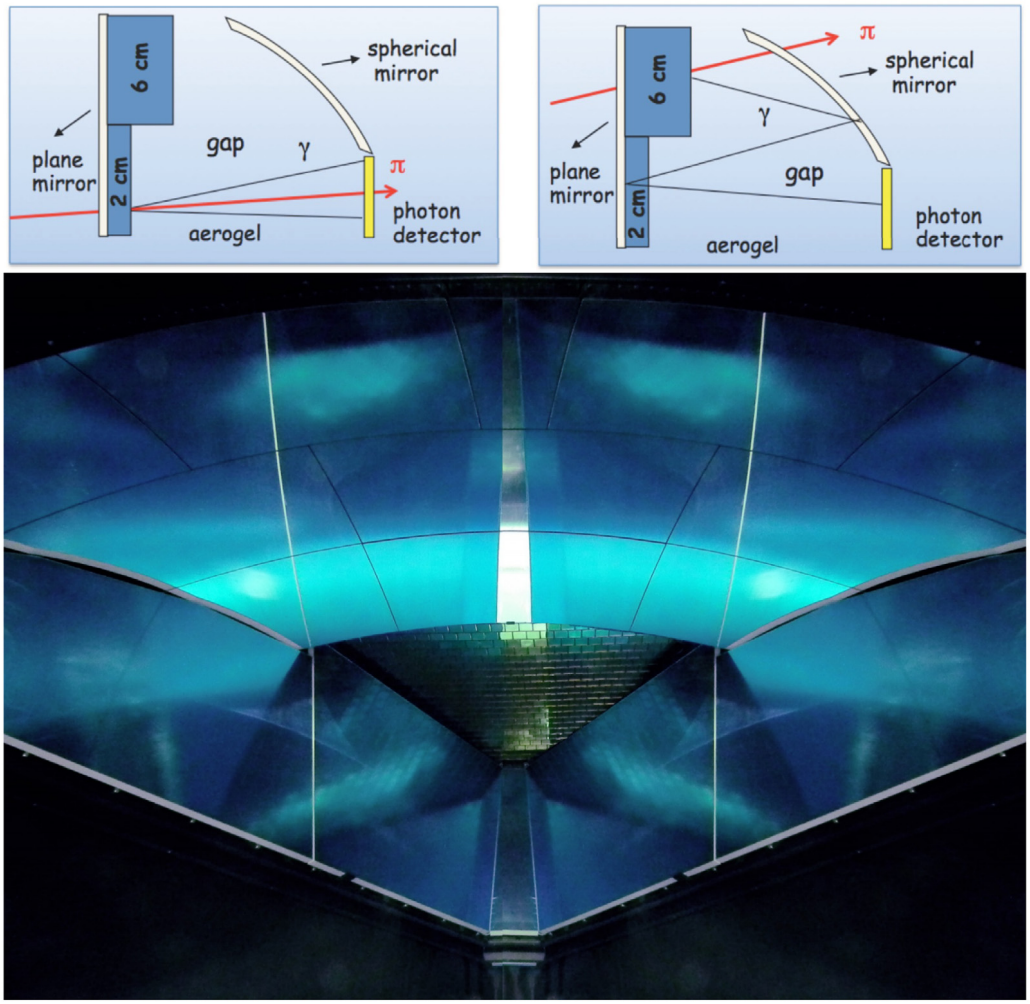

Fig. 10. Top: Optical design of the CLAS12 RICH indicating the paths of direct (left) and reflected photons (right) [33]. Bottom: Photograph of the assembled mirror system with view on the photodetector wall [34].

CsI chambers and leads to single photoelectron detection efficiency of better than 80%.

3.2.3. The CLAS12 RICH

The CEBAF Large Acceptance Spectrometer CLAS12 is part of an energy upgrade program at the Thomas Jefferson National Accelerator Facility TJNAF. A RICH [33] shall provide $\pi/K/p$ separation at momenta up to 8 GeV/c. Following the 6-fold radial sector geometry of CLAS12, the RICH combines aerogel radiators with HPK flat panel H8500 and H12700[5] MAPMTs [38] and fast readout electronics based on the MAROC3 ASIC [39]. A sophisticated system of focusing and plane mirrors, shown in Fig. 10, allows to reduce the detection area to about 1 m^2 (per sector). The 5 × 5 cm^2 large MAPMTs provide 89% active area coverage and make concentrating lenses obsolete. At this stage one sector (391 MAPMTs) is installed and operational [38]. The preliminary value of the single photoelectron Cherenkov resolution is 6 mrad and expected to improve to the design value of 4.5 mrad once corrections and calibrations are applied [40].

3.2.4. Projects under construction

GlueX DIRC — The GlueX experiment at the US Jefferson lab is currently being extended by a DIRC [41] in planar geometry recycling four bar boxes from the former BaBar [42] experiment at SLAC. A box comprises 12 quartz bars closely-packed side-by-side each of dimensions $35(W) \times 17.25(H) \times 1225(L)$ mm^3. Different from BaBar, two compact focusing optical boxes which are equipped with 90 MAPMTs of type H12700 each, read out two pairs of bar boxes mounted side-by-side. The detector is expected to provide π/K separation up to 4 GeV/c.

LHCb RICH upgrade — In the current Long Shutdown 2 (LS2) of the LHC, the LHCb experiment undergoes a major upgrade. All sub-detectors shall comply to a new 40 MHz readout scheme without hardware trigger. The pixel-HPDs that were instrumenting the LHCb-RICH detectors encapsulate the readout ASIC inside the vacuum envelope (see Section 5). Since the electronics cannot be upgraded without re-building the HPD, LHCb decided to replace in both RICHes the HPDs with ~3000 MAPMTs [43,44], profiting from the improved QE and active-area fraction of the latest MAPMT models [24]. At the same time, the optics of RICH 1 is slightly adapted. The aerogel radiator of RICH 1 was already removed in 2015.

It should be noted that, already in the late 1990s, LHCb had studied the performance of R7600-03-M64 MAPMTs as a back-up alternative to the two different HPD options under development for the readout of the two large RICH detectors [45]. The requirements and design of the LHCb and HERA-B RICH detectors have many similarities. To overcome the low active area of the R7600 MAPMT (48%) LHCb developed a concentrating optics based on a single 24 mm thick plano-convex quartz lens which led to a demagnification factor 1.5 and a 55% increase in the

[5] The H12700 differs from the H8500 by an improved dynode structure which results in a higher single photon detection efficiency.

number of detected photoelectrons. Laboratory and test beam studies yielded an excellent merit factor $N_0 = 110\ m^{-1}$ and confirmed MAPMTs to meet the photodetector requirements of LHCb.

CBM RICH and HADES upgrades — The Compressed Baryonic Matter (CBM) experiment at the future FAIR facility at GSI, Germany, will comprise a mirror-focused RICH detector, which shall provide electron–pion separation up to 8 GeV/c [46,47]. It is based on a CO_2 gas radiator and two large spherical mirrors above and below the beam axis. The 2.4 m^2 large focal plane is equipped with about 1100 MAPMTs of type H12700, already procured and successfully tested.

While waiting for the start-up of FAIR, expected around 2025, a subset of these MAPMTs (428 pieces) has been used to replace the CsI + MWPC based photo-detection system of the HADES RICH [48], since ageing phenomena during 15 years of operation resulted in a loss of about 40%–50% of its efficiency. This rejuvenation of the HADES RICH is expected to greatly boost its performance (about a factor 2 in the number of detected photoelectrons) for the physics run of the so-called FAIR phase-0 programme and provides a realistic test-bed environment for the MAPMTs and the DiRICH electronics [49] which will later on also be used for CBM and PANDA.

Table 2 gives an overview of the discussed Cherenkov imaging detectors using MAPMT photo-tubes.

4. Micro-channel plate photo-multiplier tubes

Micro-channel plate electron multipliers have been originally developed for night vision applications in the military domain [50]. These miniature devices were integrated in proximity-focussed image intensifiers (Gen II — see Fig. 11). In this way, Gen II tubes outperformed the previous generation of image tubes (Gen I) in terms of gain while keeping a comparable high spatial resolution. These features have quickly appeared to be very attractive for scientific applications. Optoelectronic systems combining Gen I and II image intensifiers have for example been used for the readout of charged-particle tracking detectors based on scintillating fibres in collider [51,52] and fixed-target [53–56] high-energy physics experiments. The front-end electronics usually consisted of Charge Coupled Devices (CCDs). In such a configuration, the overall readout speed was limited by the time response of the phosphor screens at the image intensifier output and the readout speed of CCD chips. With the emergence of fast electronics, the excellent MCP transit time spread properties combined with the single-photon sensitivity of Gen II tubes have triggered a growing interest in fast timing applications using Cherenkov light for charged particle identification.

4.1. Principle, design and construction

A MCP consists of a compact and close-packed set of miniature channel electron multipliers each acting as a continuous dynode [57]. The plate is manufactured from lead-glass billets having etchable core and non-etchable cladding. The billets are heated and drawn to small-diameter fibres that are bundled together to form hexagonal rods. These rods are subsequently drawn again and are fused together to form a MCP "boule". The boule is finally sliced at an angle in thin wafers that are further polished and chemically etched. Heat treatment follows under reducing hydrogen atmosphere to provide electrical conductivity and secondary emission properties. Electrodes generally made of NiCr are deposited on the MCP input and output surfaces. The MCP is finally pre-conditioned through an electron scrubbing process to stabilize its operation. The main geometrical MCP parameters are:

- Channel pore diameter d: 6–25 μm
- Channel length L: 400–1000 μm
- Diameter-to-length ratio α=L/d: 40–100
- Open-area-ratio OAR: 55%–65%

The ratio α basically defines the electrical characteristics of a MCP. Typical gains of a single MCP are in the range 10^3–10^4. For integration in an image intensifier tube, two MCPs are stacked in Chevron configuration that alternates their bias angle. This reduces ion feedback effects and optimizes the overall amplification gain that reaches $10^6 - 10^7$, a charge level that is detectable by appropriate front-end electronics. Due to their compact size, MCP-PMTs are essentially immune to high magnetic fields and intrinsically feature high spatial and time resolutions (~100 μm and ≤30 ps, resp.). Electron back-scattering may however occur at the MCP input and at the anode level, generating image halos [58] and tails in the TTS distributions [59]. Mitigating these effects primarily requires small gaps between the photo-cathode and the MCP input face (typically 200 μm or less) and between the MCP output face and the anode (typically 1 mm).

In the following, examples of existing and future Cherenkov detectors that exploit the high sensitivity, high-resolution imaging capabilities and excellent timing performance of MCP-PMT tubes are given.

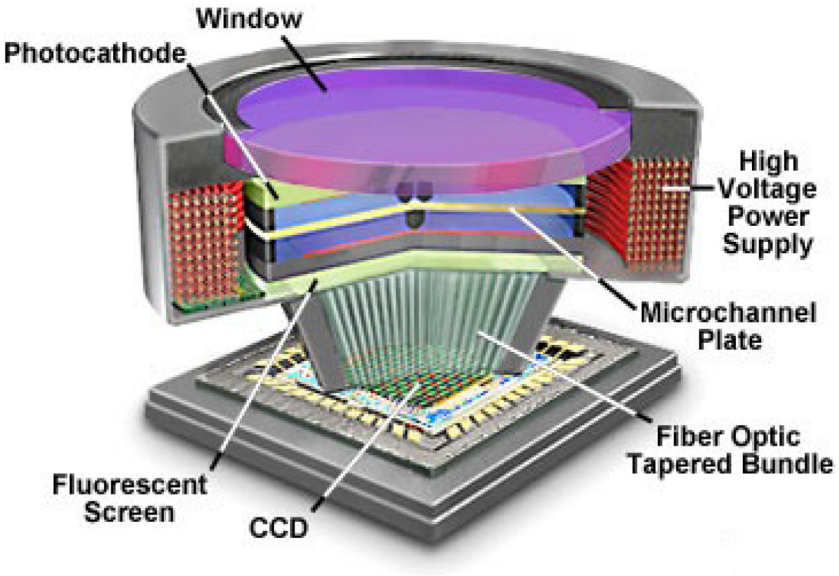

Fig. 11. Schematic 3D view of a second-generation image intensifier tube equipped with micro-channel plates [37].

Table 2
Overview of Cherenkov imaging detectors using MAPMT photo-tubes.

	HERA-B	LHCb prototype	COMPASS	CLAS12[a]	GlueX[b]	LHCb upgrade[c]	CBM
MAPMT type	R5900-M4, R5900-M16	R7600-03-M64	R7600-03-M16	H8500, H12700	H12700	R13742, R13743	H12700
pixel size (mm)	9, 4.5	2.3	4.5	6, 6	6	2.9, 6	6
Use of lenses	Yes	Yes	Yes	No	No	No	No
Start of operation	1999	≈ 2000	2006	2018	2019	2020	≈ 2025
A_{active} (m^2)	2.9	0.006	1.3	6	0.42	1.6, 2.1	2.4
N_{dev}	750, 1500	9	576	2344	180	384, 2688	1100
σ_{ph} (mrad)	1.0, 0.7		1.2	6 (prel.)	8	0.78, 0.45	
N_{pe} (for β=1)	33	n.a.	56	not yet published	20–30	40, 22	24[d]

[a]One sector installed in 2018. Numbers are for full detector (6 sectors).
[b]Performance figures based on simulation.
[c]Numbers / expectations are for RICH 1 and RICH 2 detectors.
[d]Beam test. Demonstrated 20% more by coating MAPMTs with wavelength shifter.

4.2. Applications in Cherenkov imaging

4.2.1. The imaging time-of-propagation counter of Belle II

The Belle II spectrometer at the SuperKEKB factory is designed for precision measurements of B mesons, study of rare decays, exotic-hadron spectroscopy and search for New Physics [60]. Particle IDentification (PID) in the barrel region is provided by the imaging Time-Of-Propagation (iTOP or TOP) counter [61]. Its design is inspired by the Babar DIRC [42]. The TOP counter consists of 16 modules arranged cylindrically. Each module is made of a 20 mm-thick, 450 mm-wide and 2500 mm-long quartz plate terminated at the forward end by a mirror and at the backward end by an expansion prism coupled to an array of 16 × 2 square photodetectors (Fig. 12). Cherenkov photons generated by charged particles in the plate propagate by total internal reflection. In the backward direction they reach the expansion prism and photodetectors. In the forward direction they are first reflected off the mirror before reaching the prism and photodetectors. The arrival times of the Cherenkov photons have to be measured with a resolution better than 100 ps to achieve pion–kaon separation over a momentum range 0.5–4.0 GeV/c.

The photodetectors should feature good single-photon detection efficiency, high gain, very short TTS in high axial magnetic field. They should be square-shaped to be arranged in close-packed arrays. Finally, they should survive with acceptable performance drop during the whole period of Belle II operation. To satisfy all these requirements, dedicated MCP-PMTs have been developed in close collaboration with industry.[6] The tubes have an overall size 27.6×27.6 mm^2 and an active area 23 × 23 mm^2 [62]. The photo-cathode is multi-alkali with a QE of 28% on average at 360 nm wavelength. The amplification is provided by a stack of two 400 μm-thick MCPs with 10 μm pore size. The tube anode is segmented as an array of 4 × 4 pads each 5.3×5.3 mm^2 in size. At nominal operating voltage (3 kV), the gain is 10^6 and TTS is in the range 30–40 ps. The gain drops to 5×10^5 and the TTS stays below 50 ps when the tube is operated in a 1.5 T axial magnetic field. The tube lifetime is defined as the value of Integrated Anode Charge (IAC) for which the relative photo-cathode QE drops by 20%. Initial simulations predicted that IAC would reach 2–3 C/cm^2 over the Belle II operation. A comprehensive MCP R&D programme was started to satisfy the requirements. Conventional MCP-PMTs show severe degradation caused by ion feed-back in terms of gain and QE. Their performance drops for IAC values exceeding a few tens or hundreds mC/cm^2. The tube lifetime was first improved by the insertion of a thin Aluminium film between the first and second channel plates. In this position, the film mitigates ion feed-back effects without compromising the collection efficiency of the primary photoelectron. This resulted in so-called "conventional" MCP-PMTs with stable operation up to 1 C/cm^2 [63]. Lifetime was further extended to 3–10 C/cm^2 by applying an additional Atomic Layer Deposition (ALD) process [64] on the MCPs. This 3-step process consists of the successive deposition of a resistive layer, a secondary-emission layer and an electrode layer. Since these layers are intrinsically very different, their performance can be independently optimized. The most recent TOP tubes with ALD-processed MCPs exhibit lifetimes reaching 20 C/cm^2 [65]. These latter developments were motivated by more severe background estimates in Belle II [66].

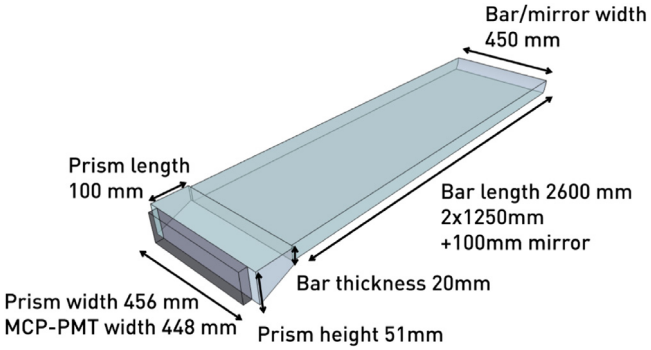

Fig. 12. Schematic of a TOP module of Belle II [67].

Over 600 MCP-PMTs have been produced in three categories labelled "conventional", "ALD" and "life-extended ALD" and related to the tube lifetime. The TOP counter fully instrumented with 512 tubes has been assembled and installed in Belle II [66,69] (Fig. 13). The front-end electronics readout is based on a dedicated high-frequency waveform-sampling ASIC [70]. The ASIC integrates a 11 μs-long analogue buffer compatible with the trigger latency (5 μs) and the maximum average trigger rate of 30 kHz expected in nominal luminosity conditions (8×10^{35}/cm^2). The TOP counter has been successfully operated with first beam collisions [67,71]. Particle identification tests have been performed and are illustrated in Fig. 14. The distribution of photon arrival time in each readout channel is compared with the expected distributions for various particle hypotheses. In the present case, the space–time distribution is clearly associated to a kaon candidate.

4.2.2. Projects under construction or in R&D phase

The PANDA Barrel DIRC and End-cap Disc DIRC counters — The PANDA experiment at FAIR is currently under construction [72]. It will be using collisions between an anti-proton beam and a hydrogen or hyper-nuclear cluster jet target to explore fundamental properties of strong interactions. Particle identification in PANDA will primarily be achieved by two DIRC-like counters [73]: the Barrel DIRC [74] and the End-cap Disc DIRC [75]. All optical elements are made of fused synthetic silica. The Barrel DIRC design is closely related to that of the Babar DIRC [42]. Sixteen sectors are arranged cylindrically around the beam pipe with each sector comprising a bar box and an expansion prism (Fig. 15). The box contains three 17 mm-thick, 53 mm-wide, 2400 mm-long bars placed side-by-side and separated by a small air gap. Flat mirrors terminating the bars on one end reflect Cherenkov photons towards the readout end. These photons are subsequently

[6] HPK.

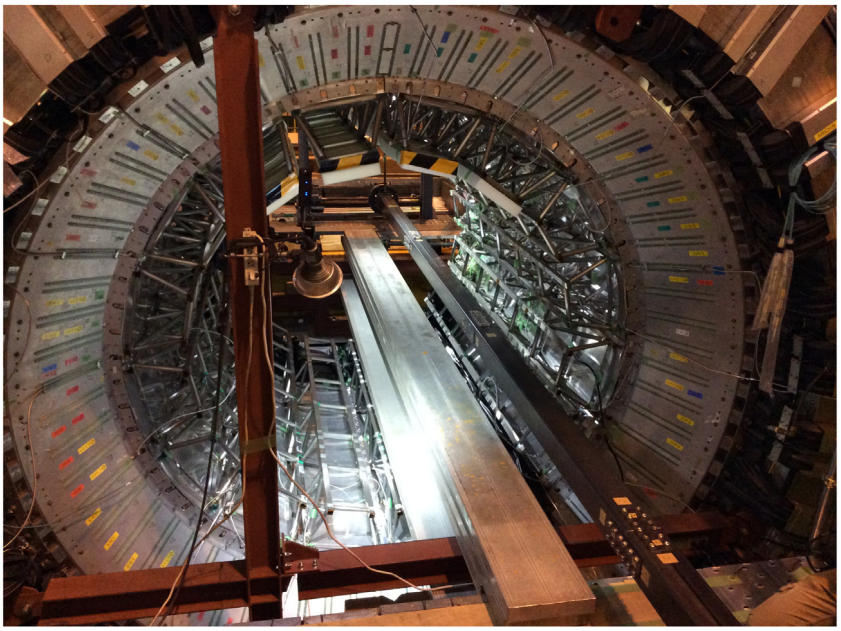

Fig. 13. The TOP detector system after installation in Belle II [68].

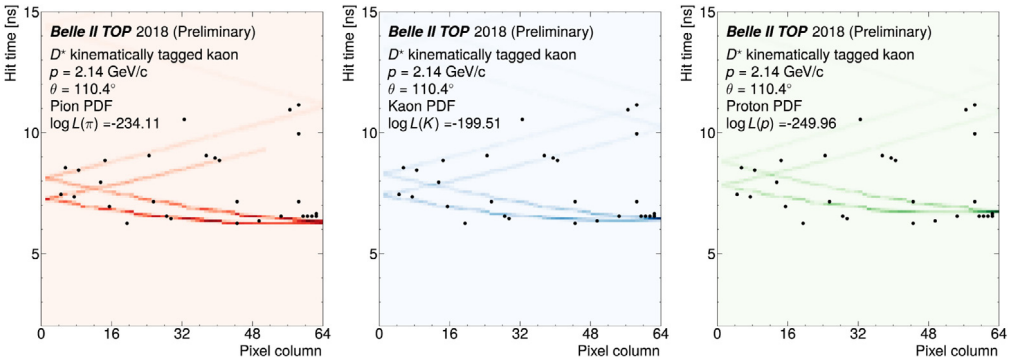

Fig. 14. Time–space distribution of hits (black dots) recorded by the TOP counter of Belle II. The expected patterns from a pion (left), a kaon (centre) and a proton (right) are superposed. The hits are associated to a kaon candidate [67].

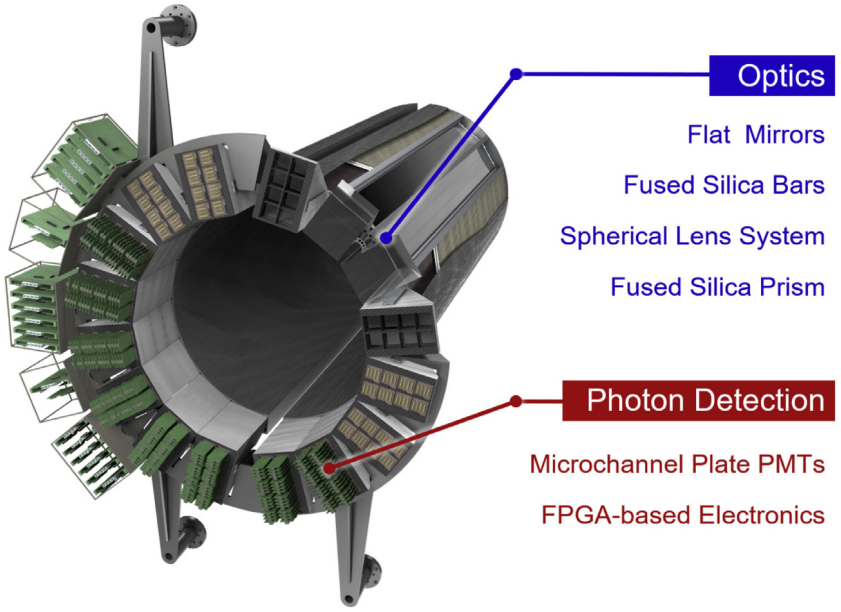

Fig. 15. Schematic 3D view of the PANDA Barrel DIRC [73].

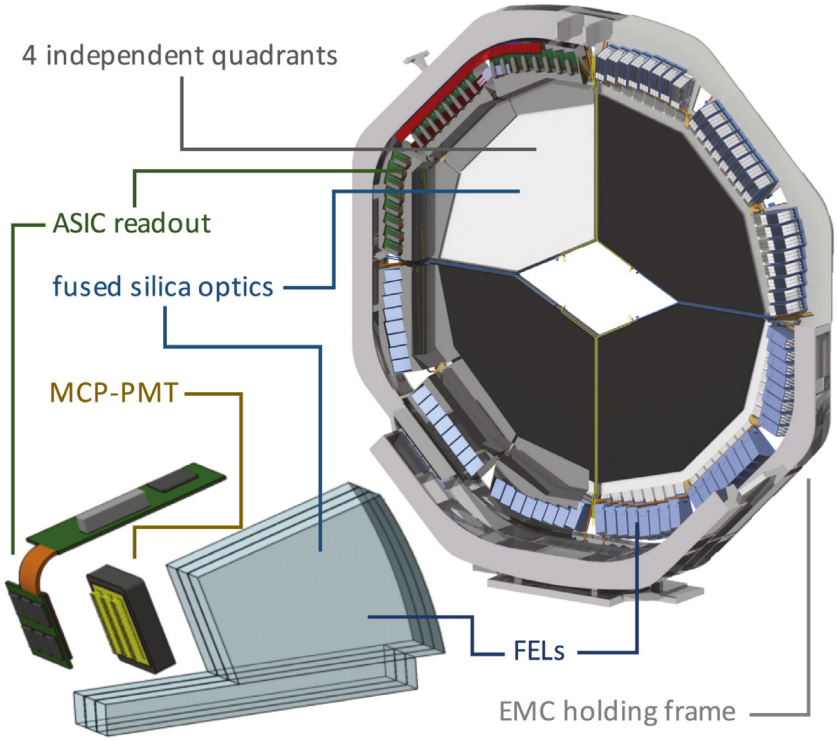

Fig. 16. Schematic 3D view of the PANDA End-cap Disc DIRC and the inside of a readout module [73].

focussed via a lens to the expansion prism and detected by an array of MCP-PMTs.

The End-cap Disc DIRC is divided in four quadrants each consisting of a 20 mm-thick radiator and 24 readout modules (Fig. 16). A readout module contains three bars and three focussing elements, one MCP-PMT and its front-end electronics readout board.

The MCP-PMTs have to satisfy the following PANDA requirements [76]:

- Compactness, low noise and radiation hardness
- Operation in a 1 T axial magnetic field
- Anode segmentation: $\sim 6 \times 6$ mm^2 (Barrel DIRC) $\sim 0.5 \times 16$ mm^2 (End-cap Disc DIRC)
- Photon arrival time precision: 100 ps
- Single photon rate: ~ 1 MHz/cm^2
- Integrated anode charge IAC: >5 C/cm^2

The last stringent requirement on integrated anode charge motivated the PANDA Collaboration to establish comprehensive studies and measurements on MCP-PMT ageing effects. Progress from several tube manufacturers[7] is being continuously followed up and monitored in a dedicated test facility [77]. Results from some latest tube prototypes show lifetimes in excess of 10–20 C/cm^2 with no degradation of QE or MCP gain (Fig. 17).

Various MCP-PMT tube candidates with long lifetime and the two segmentations required for PANDA DIRCs have been made available. PANDA DIRC prototypes instrumented with these tubes have been validated through a series of beam test campaigns using mixed particle beams at CERN [78]. The readout electronics is developed in common with the HADES and CBM heavy ion spectrometers [49,79]. It is based on amplifier-discriminator front-end chips providing time-over-threshold information, and time digitizers implemented in field-programmable gate arrays. An example of barrel DIRC photon pattern measured with a matrix of 8 × 8-channel 2 inch MCP-PMTs is reproduced in Fig. 18. Similar patterns have been recorded with an End-cap Disc DIRC prototype instrumented with 2 inch MCP-PMTs of spatial segmentation 3 × 100 pixels and 0.5 mm fine pitch.

The TORCH detector project for LHCb — The Timing Of internally Reflected CHerenkov photons (TORCH) is a time-of-flight detector for particle identification at low momentum [80]. It is proposed to complement the PID capabilities of the LHCb experiment currently provided by two gaseous RICH detectors [11]. The TORCH detector consists of 18 flat modules placed side-by-side in a vertical plane and located in front of the downstream RICH 2 detector. Each module comprises a rectangular quartz radiator plate 10 mm thick, 660 mm wide and 2500 mm long. Cherenkov photons generated in a plate propagate by total internal reflection to the edge where cylindrical focusing optics map the photon angle in the transverse plane to the finely-segmented direction of the photon detectors (Fig. 19). The other coarser segmentation provides the photon angle in the longitudinal plane. This segmentation corresponds to a 1 mrad angular precision that is required to achieve an overall per-photon time precision of 70 ps [80].

The basic requirements for the TORCH photodetectors are summarized below:

- Compactness, low noise and radiation hardness
- Operation in a 10 mT magnetic field
- Anode segmentation: $\sim$128×8 pixels for a 2 inch square MCP-PMT
- Overall per-photon time precision: 70 ps
- Single photon rate: $\sim$1–10 MHz/cm^2
- Integrated anode charge IAC: 10–20 C/cm^2

The upper limits for the last two items refer to central TORCH modules where particle track occupancies are expected to be the highest. To validate the TORCH concept and the performance of basic elements, a comprehensive R&D programme has been carried out within the framework of a EU-funded collaboration.[8] The programme involved an industrial partner[9] for the photodetector development [82] that was

[7] Photonis, HPK, Photek Ltd., BINP.

[8] FP7 Advanced Grant ERC-2011-AdG-299175-TORCH.

[9] Photek Ltd.

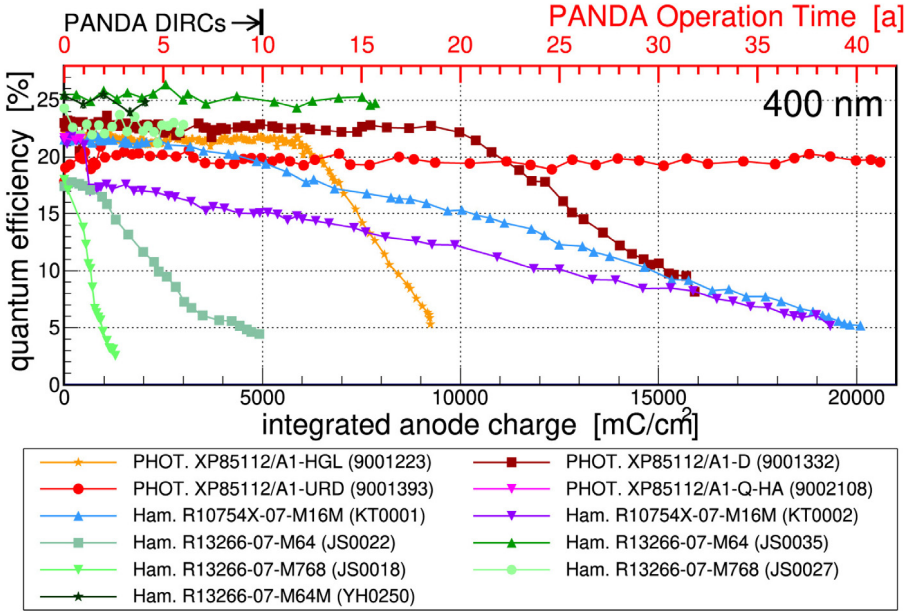

Fig. 17. PANDA lifetime measurements of ALD-coated MCP-PMTs from several manufacturers — The curves display QE at 400 nm vs IAC [76].

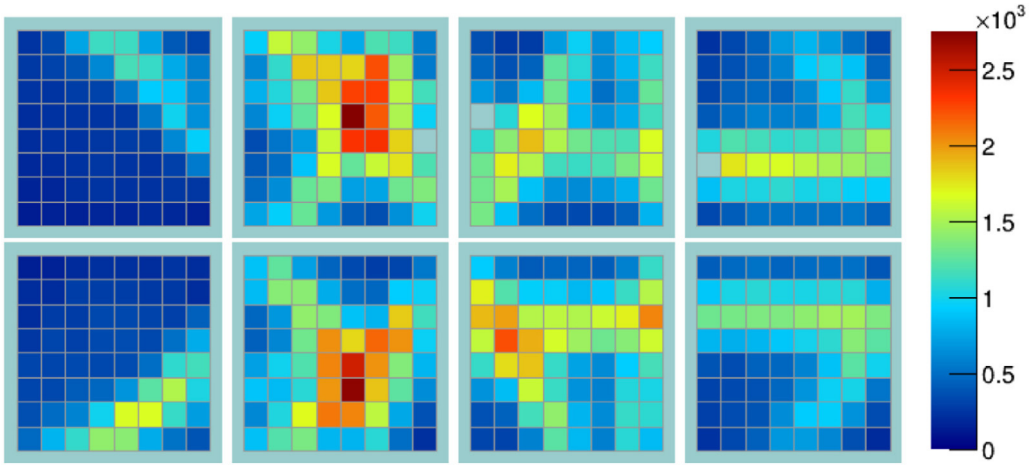

Fig. 18. Photon patterns measured with a 7 GeV/c pion beam on a PANDA Barrel DIRC prototype. The patterns result from multiple reflections of Cherenkov photons during their propagation in the quartz radiator bars [78].

organized in three phases [83]: phase I was devoted to the manufacture of circular single-channel MCP-PMTs processed with ALD for lifetime studies. In phase II, circular MCP-PMTs were made available with a quarter-size anode having the required granularity. Phase-III TORCH MCP-PMT prototypes combined the required lifetime and anode segmentation (Fig. 20). These final tube prototypes are each 53×53 mm^2 in active area and buttable linearly with a 60 mm pitch to optimize the overall photon coverage. The micro-channel plates are processed with ALD. The anode segmentation is 64×8 pixels. While the fine granularity is increased by a factor of two, the spatial resolution originally required for TORCH is recovered through the use of charge-sharing effects across pixels and the estimate of charge centroids. Connectivity between highly-segmented anode output pads and readout electronics interface boards is achieved by the use of anisotropic conductive films, an interconnect technology that is commonly used in liquid crystal display manufacturing. The readout electronics implement the NINO front-end chip and the HPTDC ASIC [84] operated in high-resolution mode (100 ps binning).

A first "mini-TORCH" prototype equipped with a small-scale quartz radiator plate of size $10 \times 120 \times 350$ mm^3 has been extensively tested in a mixed particle beam at CERN with phase-II [85] and phase-III [81] MCP-PMT prototypes. Photon patterns and the resulting per-photon time resolution recorded with phase-III prototypes are reproduced in Fig. 21. Time distributions have resolutions between 100 and 125 ps with a tail attributed to imperfect calibrations, back-scattering effects in the MCP-PMTs and limitations imposed by the HPTDC time binning. A second "proto-TORCH" prototype equipped with a full-width (660 mm) half-length (1250 mm) quartz radiator plate has been recently tested in a particle beam [86]. The best achieved time resolution is below 90 ps and approaches the TORCH target.

5. Hybrid photon detectors

Hybrid photon detector tubes combine vacuum photo-cathode technology with solid-state technology [87]. In an HPD, the phosphor screen of a standard image intensifier or the dynode chain of a conventional PMT are replaced with a semi-conductor detector device. While the original HPD concept is old and dates from the late 1950's [88], the emergence of reliable HPD devices was only made possible decades later with the progress on semi-conductor technology and the improved

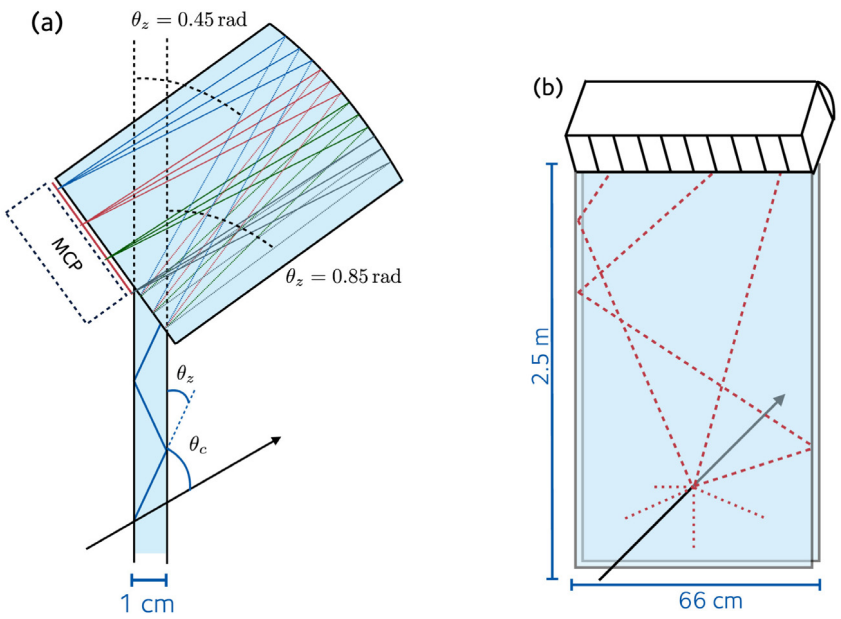

Fig. 19. Schematic of a TORCH module: (a) radiator plate edge, focussing block and MCP-PMT, (b) single TORCH module [81].

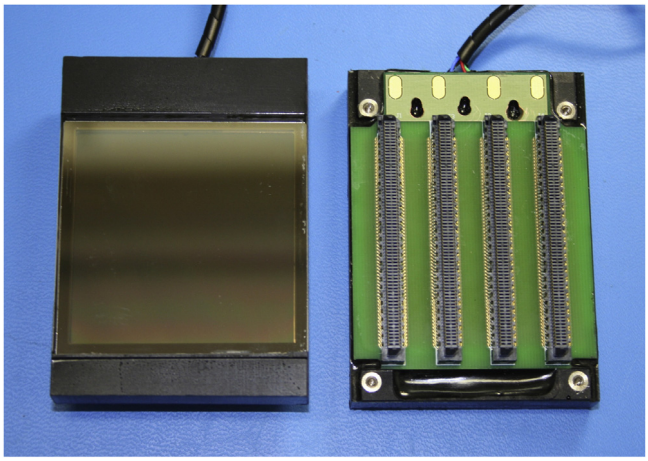

Fig. 20. Front view (left) and rear view (right) of phase-III MCP tubes developed for TORCH. The rear side is equipped with a custom printed circuit board interfacing with TORCH readout electronics [83].

compatibility with vacuum tube technology [89]. Close collaboration with industry[10] has also shown to be essential. The attractive features of HPDs such as gain uniformity, low gain fluctuations, linearity, low noise, high speed and high-resolution photon counting capabilities have triggered applications in high-energy physics for calorimetry [89,90] and RICH detectors. This latter field will be given attention in the following sections.

5.1. Principle, design and construction

An HPD is a vacuum photon detector where a primary photoelectron released from the tube photo-cathode is accelerated by an applied high voltage of 10–20 kV onto a semi-conductor detector generally made of reverse-biased silicon diode(s). The photoelectron kinetic energy is dissipated in the semi-conductor through electron–hole pair creation and phonon (lattice vibration) excitation. Electron–hole pairs are created on average for every 3.6 eV of dissipated energy. There is also energy lost (typically less than 1 keV) in the ohmic contact of the diode. The resulting gain G is rather modest and in the range 3–5×10^3. This one-step signal-generation process results in very low *intrinsic* gain fluctuations $|\Delta G| = \sqrt{F \times G}$ with a Fano factor F value 0.12. Photoelectron back-scattering effects at the detector surface affect the gain uniformity. A ∼18% fraction of photoelectrons undergo back-scattering, and release on average half of their energy at the first impact. Back-scattered photoelectrons yield lower signals and degraded time and space resolutions. The anode of an HPD can be equipped with single diodes, pad arrays of millimetre-size elements or pixel arrays of sub-millimetre-size elements. The *overall* signal fluctuations are dominated by the readout electronics noise. Appropriate coupling between the detecting elements and the input stage of the readout electronics is consequently essential. For high-speed applications where a large number of channels per HPD is required, the front-end electronics can be encapsulated in the tube vacuum. This configuration, together with small detecting elements, is optimal in terms of noise. It has however many implications for what regards the compatibility with vacuum-tube manufacturing steps. Hybrid photon detectors exist in various electron-optics configurations (proximity-, cross- and fountain-focussing) and are commercially available.

5.2. Applications in Cherenkov imaging

5.2.1. The pixel hybrid photon detectors for the LHCb-RICH counters

Particle identification in the LHCb experiment at the LHC is based on two RICH detectors with fluorocarbon gaseous radiators [11]. Cherenkov photons reflected off spherical and flat mirrors are focussed on photon detection planes covering a total surface of ∼3.3 m^2. The photodetectors must comply with the following specifications:

- Low noise and radiation tolerance
- Operation in a 1–3 mT magnetic field
- Single-photon sensitivity over 200–600 nm wavelength range
- Granularity at the photo-cathode level: 2.5×2.5 mm^2
- Time resolution compatible with LHC bunch-crossing rate (40 MHz)
- Overall active area coverage: 65%

The LHCb-RICH collaboration investigated three options to select a photodetector satisfying all above requirements. The first option

[10] Photonis (formerly DEP. B.V.), HPK.

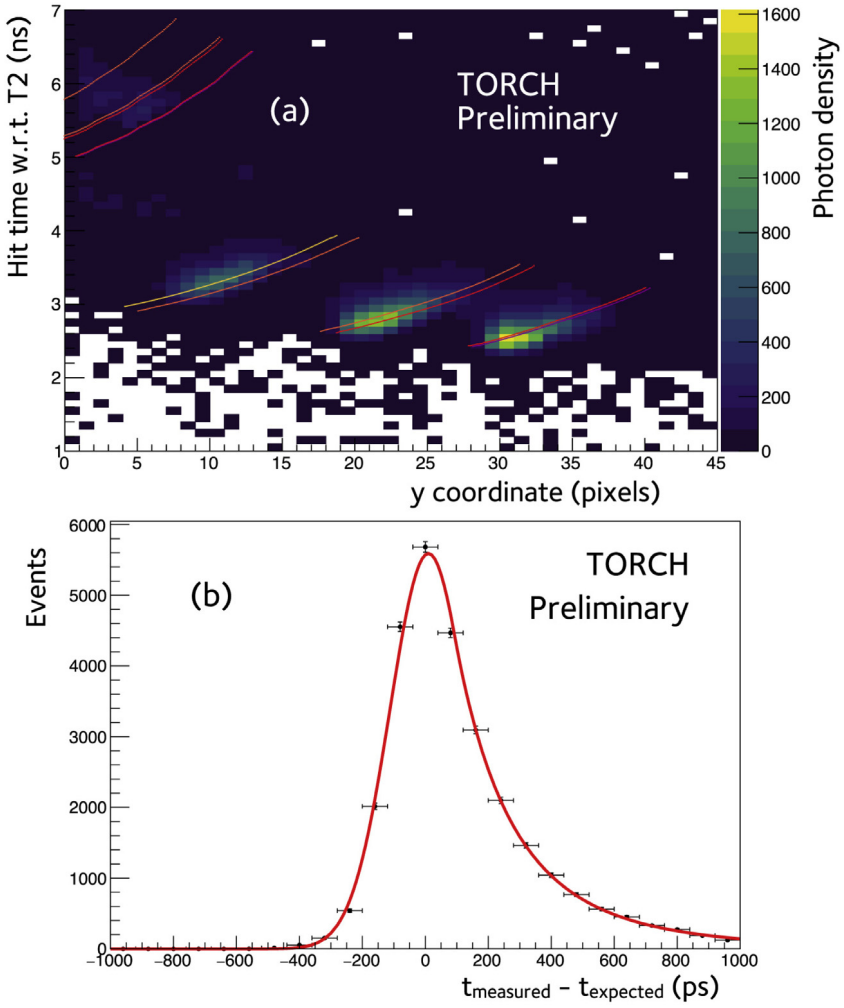

Fig. 21. (a) Time–space photon patterns measured with a 5 GeV/c pion beam on a TORCH prototype equipped with a small-scale radiator plate and instrumented with phase-III MCP-PMT prototypes. (b) Residuals between observed and simulated Cherenkov photon arrival times [81].

Fig. 22. Photograph of the 10 inch TOM-HPD (left) and the 5 inch Pad-HPD (right).

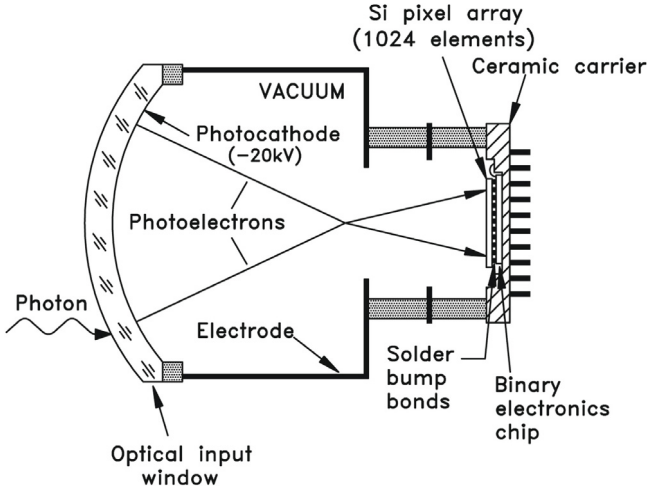

Fig. 23. Schematic of the pixel-HPD developed for the LHCb-RICH detectors [91].

already mentioned in Section 3 used commercial MAPMTs[11] equipped with lenses to compensate the low active area [45]. The second and third options were based on dedicated developments of HPDs with segmented anodes and encapsulated readout electronics. They are detailed in the following paragraphs.

[11] Model R7600 from HPK.

Fig. 24. Pixel-HPDs installed in the upper box of the LHCb-RICH 1 detector.
Source: Picture source CERN.

Even if it not crowned by an application in a HEP experiment, Tom Ypsilantis and Jacques Séguinot made also pioneering and innovative contributions in the field of HPD development. They initiated in the mid-1990s the development of a 5 inch (127 mm) HPD with encapsulated readout electronics called Pad-HPD [92,93]. The tube shown on the right in Fig. 22 was intended to instrument the detection planes of the two LHCb RICH detectors. A set of four ring electrodes defined a fountain-shaped electrostatic configuration, which de-magnified the photo-cathode image by a factor 2.5 onto a silicon sensor of 50 mm diameter. The sensor comprised 2048 pads of size 1×1 mm^2 and was read out by multiplexed analogue electronics (16 IDEAS[12] VA3 ASICs with 128 channels each). The HPD was fabricated in a dedicated ultra-high vacuum photo-cathode facility [13] at CERN which had been designed and built for this purpose. When the LHCb collaboration decided in 1999 to instrument its RICH detectors with the Pixel-HPD (see below), the CERN facility was used to develop a number of HPD prototypes targeting applications in (astro) particle physics and medical imaging, including a 10 inch HPD for cosmic ray imaging. In memory of Tom Ypsilantis, this latter HPD tube was baptized TOM-HPD [94] (on the left in Fig. 22).

Finely-segmented pixelized HPDs (pixel-HPDs) were selected as LHCb-RICH photodetectors. These tubes have been specifically developed in collaboration with an industrial partner.[13] Pixel-HPDs followed previous developments started with the same company. The concept of an HPD with encapsulated pixel detector and readout electronics was demonstrated in 1994 [95] and validated with cosmic rays and in a particle beam using a small-diameter scintillating fibre target. The first observation of Cherenkov ring images from aerogel, air and C_4F_{10} gas radiators in a LHCb-RICH beam-test prototype using HPDs was reported in 1998 [96]. The HPDs were proximity-focussing tubes with 18 mm active diameter, 61 hexagonal pads each 2 mm flat-to-flat in size and external readout electronics. The front-end electronics used the analogue IDEAS VA2 ASIC (1.2 μs peaking time). Pixel-HPDs are larger cylindrical tubes with 72 mm active diameter and cross-focussing electron optics that demagnify the photo-cathode image by a factor of ∼5 (Fig. 23). The tube active area is 80%. The multi-alkali photocathode is deposited on a spherical quartz input window to optimize quantum efficiency (30%–35% at 270 nm) and minimize chromatic dispersion effects from the gas radiators. The tube design, electron-optics and detection efficiency were validated in the laboratory with a phosphor screen prototype and in beam tests with three HPD prototypes equipped with 61-pad anodes and external VA2 readout [97].

Final pixel-HPD prototypes [91] encapsulated a small silicon detector array of 32×32 pixels each $500\ \mu m \times 500\ \mu m$ in size. The pixel detector is bump-bonded to a custom binary readout chip with matching pixel electronics having 25 ns peaking time [98]. This flip-chip assembly is mounted in a ceramic carrier. Close coupling of detector and front-end readout followed by encapsulation in the tube vacuum optimizes the signal-to-noise ratio. This design option however requires full compatibility with vacuum tube manufacturing steps that include bake-out cycles at high temperature (typically 350 °C for 5–6 h). A high-temperature bump-bonding process using 10%Sn-90%Pb solder was specially developed for that purpose [99]. The binary chip architecture is actually based on the readout of sub-pixels of size $500\ \mu m \times 62.5\ \mu m$. The small sub-pixel size results in a low rms noise of typically ∼140 e with a discriminator threshold set at 1000 e. An internal logic subsequently groups sub-pixels by 8 in order to comply with the LHCb readout architecture (trigger latency 4 μs and maximum trigger rate 1MHz). The mode of operation reading out all sub-pixels is slower and is only used for calibration and monitoring purposes.

In total, 550 pixel-HPDs have been manufactured [100], and 484 units have been installed in the LHCb-RICH detectors [101] (Fig. 24). Cross-focussing optics are susceptible to magnetic distortions in low field amplitudes. To mitigate this effect, each tube is surrounded with an individual cylindrical shield made of ferromagnetic material. Pixel-HPDs were operated at 16–18 kV and resulted in typical gains in

[12] Integrated Detector Electronics AS – IDEAS, NO-0484 Oslo, Norway.
[13] Photonis (formerly DEP B.V.).

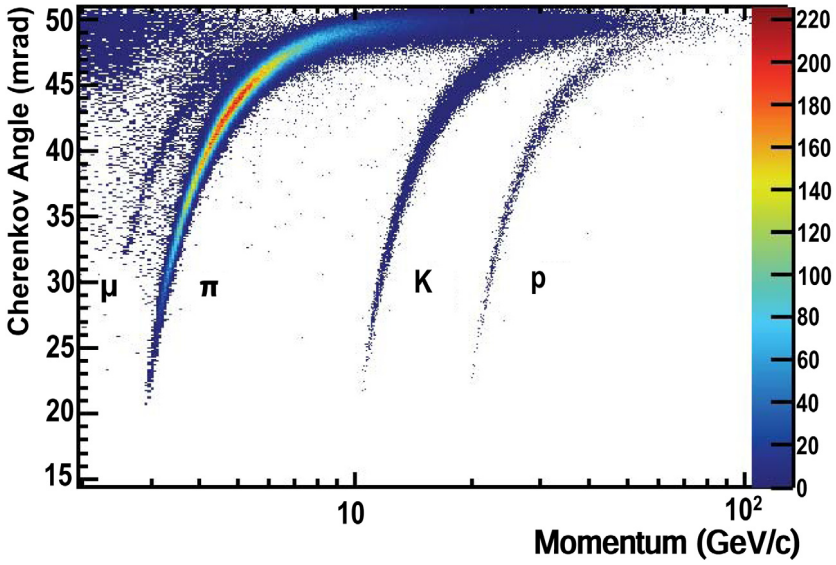

Fig. 25. Reconstructed Cherenkov angle as a function of track momentum in the LHCb-RICH 1 C_4F_{10} radiator [2].

the range ~4–5×10^3. Clear and noise-less Cherenkov photon signals were recorded. A sub-set of pixel-HPDs suffered from ageing effects caused by ion-feed-back [102]. This lifetime issue was solved by the implementation of getter strips during the re-processing of degraded units that subsequently showed full vacuum stability.

During the 10 years of LHCb operation (LHC Runs I and II), the LHCb-RICH detectors have been optimally and stably operated [2,103]. They have proved to be a key ingredient to the successful physics programme delivered by the LHCb experiment. The quality of these detectors is illustrated in Fig. 25 that shows the reconstruction of Cherenkov angles for various charged particle species detected in the RICH 1 radiator.

5.2.2. The hybrid avalanche photon detectors for the aerogel ring imaging Cherenkov detector of Belle II

Particle identification in the Belle II spectrometer has been introduced in Section 4 with the TOP detector installed in the barrel region. The same PID functionality over the momentum range 0.5–4.0 GeV/c is provided in the forward end-cap region by the Aerogel Rich Imaging CHerenkov (ARICH) detector [104]. The ARICH detector consists of an aerogel radiator and an annular photodetector system located 20 cm away. Charged particles traversing two adjacent layers of aerogel with increasing refractive indices (1.045 and 1.055) generate Cherenkov photons that are subsequently proximity-focussed at the photodetector plane (Fig. 26). This 2-layer design is providing a larger number of photons while preserving the Cherenkov angle resolution of a single layer.

Photodetectors for ARICH must comply with the following requirements:

- Compactness, low noise and radiation hardness
- Immunity to 1.5 T axial magnetic field
- Single-photon sensitivity optimized at 400 nm
- Two-dimensional position precision: 5 mm

Hybrid Avalanche Photon Detectors (HAPD) have shown to satisfy the above requirements [105]. The high collection efficiency of HAPDs is in particular compensating the rather modest light yield from aerogel. These photodetectors have been developed with industry.[14] They are in the form of square tubes $73 \times 73\text{mm}^2$ in size and 28 mm in height. The optical input window is made of quartz and the photo-cathode is of the

[14] HPK.

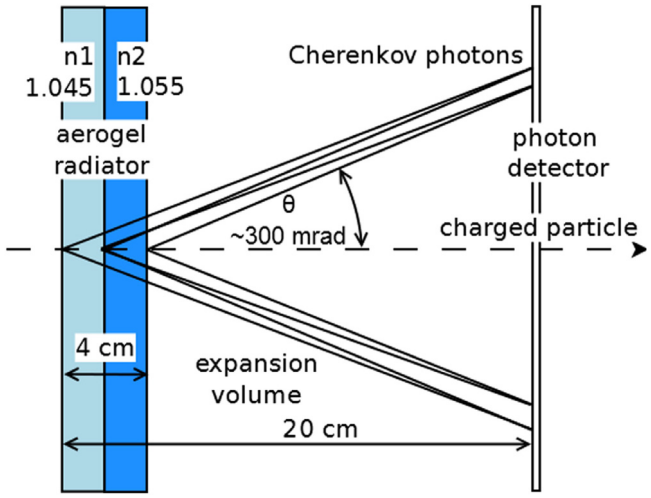

Fig. 26. Schematic principle of the ARICH detector of Belle II: Cherenkov photons generated in two aerogel tiles with increasing refractive indices are proximity-focussed on the same ring and detected by position-sensitive photon detectors [104].

"super bi-alkali" type. Typical peak QE values reach 28%. The tube anode encapsulates four closely-packed arrays of avalanche photodiodes. An array is composed of 6 × 6 pads each $4.9 \times 4.9\text{mm}^2$ in size. Photoelectrons are accelerated towards the avalanche sensor where they generate charge signals through a combined bombardment and avalanche process. Typical bombardment and avalanche gain values are 1500 and 40, resp. In comparison with standard photodiodes, the additional avalanche gain results in an overall gain of ~6×10^4 that relaxes the design specifications of the front-end readout ASIC. Cherenkov photon hit information is electronically processed through three stages: pre-amplifier with adjustable gain, stretcher with adjustable shaping time (typical value 100 ns) and comparator [106]. Operation in high magnetic field resulted for some HAPDs in the generation of high-amplitude signals inducing dead time, electronics upsets and degraded performance [107]. These issues were suspected to be caused by the HAPD vacuum quality. They have since been much reduced through a reactivation of the getter implemented in each HAPD [105].

More than 500 HAPDs have been manufactured and tested out of which 420 have been mounted in the ARICH detector to instrument 248 aerogel tiles (Fig. 27). Installation of ARICH in Belle II was

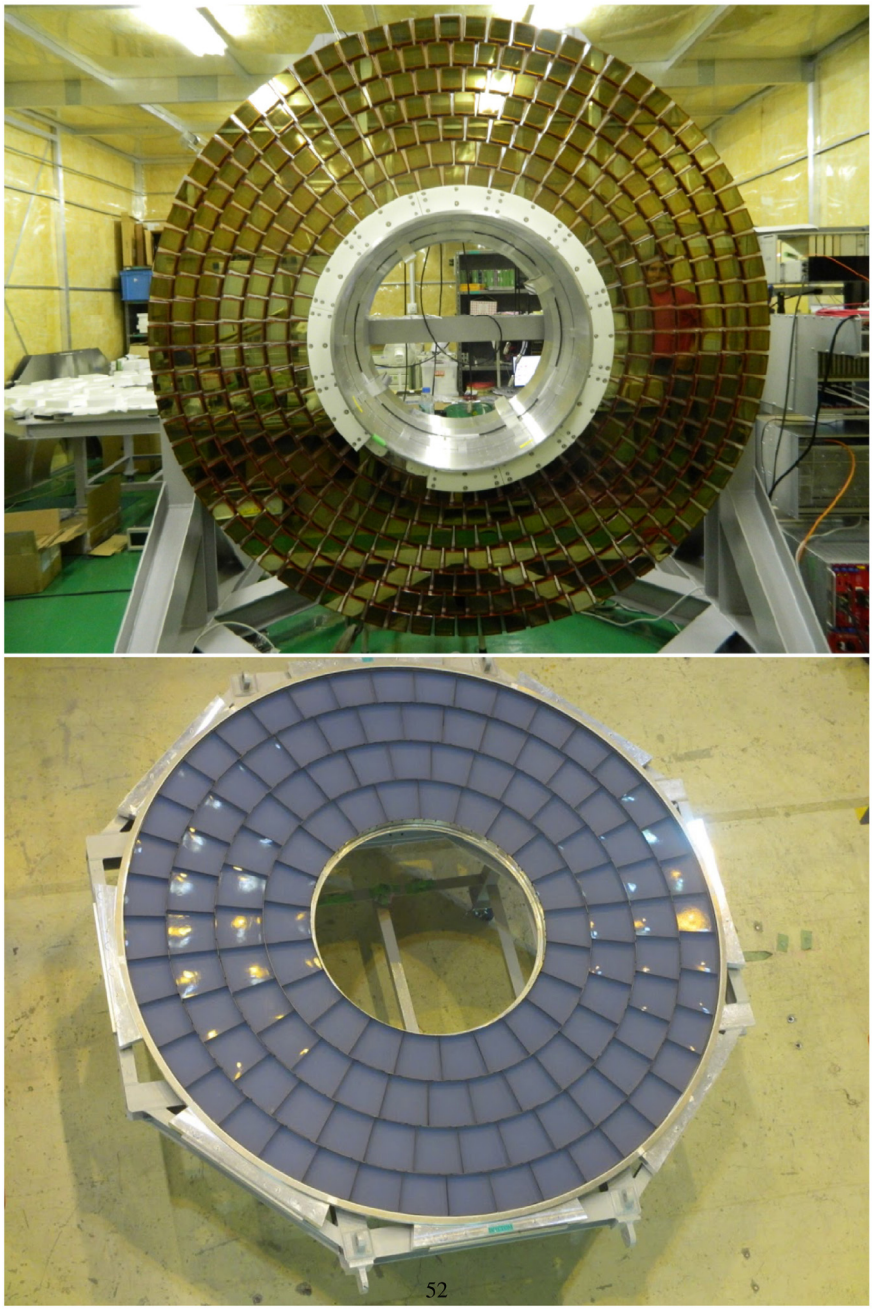

Fig. 27. Assembly of the Belle II ARICH detector. Top: photon detector plane with HAPD sensors; bottom: aerogel radiator plane [60].

followed by commissioning activities with cosmic rays and beam collisions [108]. Clear aerogel rings generated by Bhabha electrons have been recorded [109]. The corresponding Cherenkov photon angular distribution is reproduced in Fig. 28.

6. Summary and outlook

Position-sensitive vacuum photon detectors are a mature and reliable technology. As illustrated in the present paper, these devices have successfully instrumented various large-scale detectors for Cherenkov light imaging where single-photon sensitivity is mandatory. They remain unsurpassed in terms of intrinsic noise and radiation hardness.

Multi-Anode PMTs have over the last two decades evolved towards very high-performance devices, finding applications in several existing and future Cherenkov imaging detectors. The evolution of this species is hard to predict as HPK is the only producer. While adaptations of design parameters to a specific application are in principle always possible, HPK does not seem to have new MAPMT generation in the pipeline. More recently, HPK demonstrated a completely different miniaturization approach that makes use of a quasi-planar dynode structure produced from a silicon wafer, which is sandwiched between two glass plates. This so-called microPMT [110] (Fig. 29) has no longer a tubular shape but still relies on the classical PMT principle, i.e. it multiplies secondary electrons in a dynode structure made of discrete elements to a gain of around 10^6. The complete device has dimensions $13 \times 10 \times 2$ mm^3, with the photo-cathode covering 3×1 mm^2 area. While such a device should find ample applications in numerous life-science and industrial domains, the low active-area fraction in current implementations of this concept makes it not yet interesting for Cherenkov imaging applications. However, it shows how new fabrication technologies can open up ways for new concepts, designs and applications.

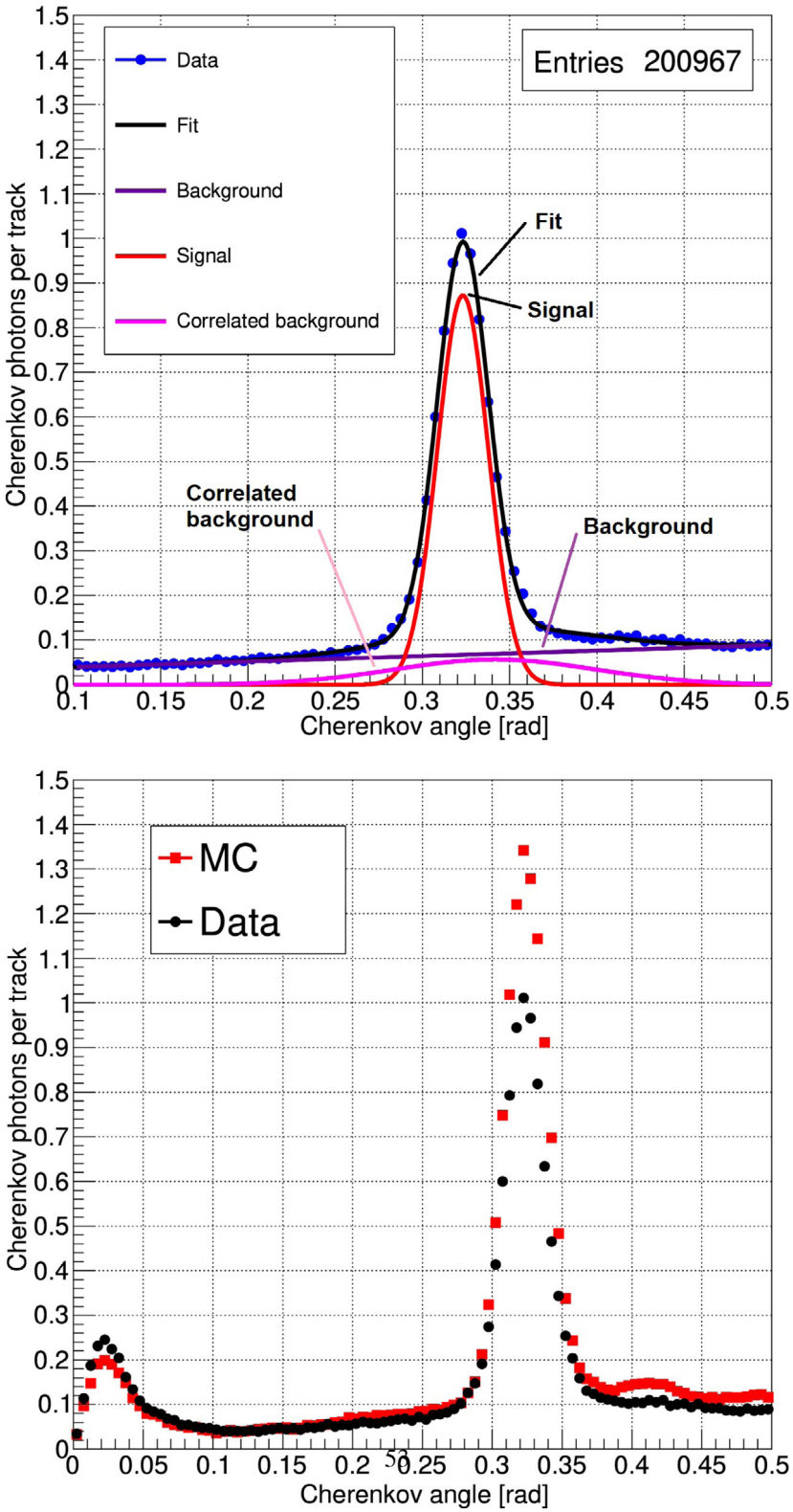

Fig. 28. Cherenkov photon angular distribution recorded in the Belle II ARICH detector: (top) data from Bhabha electrons, (bottom) comparison between data and Monte-Carlo simulation [109].

Commercial MCP-PMTs offer improved performance, longer lifetimes and an increased number of anode pads with smaller dimensions. In parallel, large-area MCP-PMTs based on borosilicate micro-capillary substrate and ALD technology have undergone significant enhancements over the last several years [112,113]. These features motivate the use of MCP-PMTs for new detector concepts such as those investigated for the future Electron Ion Collider [114]. Particle identification over a wide momentum range will be achieved by a high-performance DIRC [115] and dual-radiator and modular RICH detectors [116] with MCP-PMTs as the currently preferred option for the photodetectors.

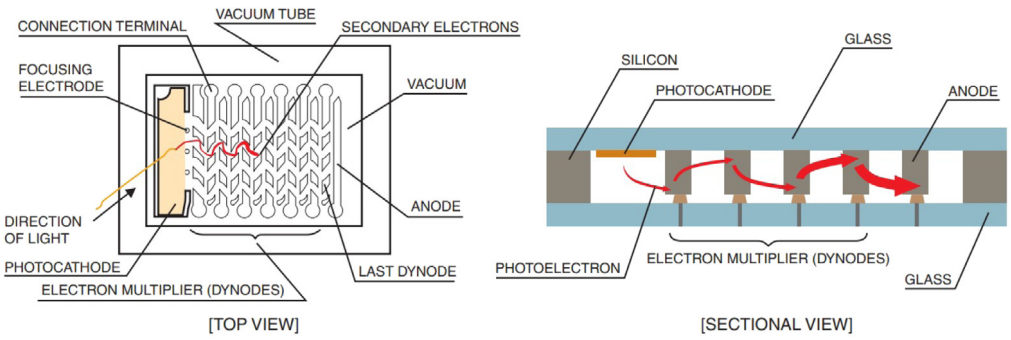

Fig. 29. Internal structure and principle of operation of a microPMT [111].

The performance of HPDs with encapsulated electronics is in constant evolution, in particular for what regards spatial and time resolutions. Electron-bombarded CCDs are since long commercially available and combine the single-photon sensitivity of vacuum photon detectors and the fine granularity of CCD chips. They are routinely used in various applications such as fluorescence microscopy for imaging labelled cells in single photon counting mode [117]. Conventional CCDs have however rather limited readout speed and may be replaced with custom CMOS devices electron-bombarded on their back side. CMOS sensors have pixel noise as low as 1 e, and faster readout frame rates [118]. Increased demands for finely-segmented devices coupled to ultra high-speed electronics motivate more specific HPD tube design studies and developments. These devices encapsulate a standard amplification stage (stack of two MCPs in Chevron configuration) and high-performance pixel readout ASICs at the anode [119,120]. Output charge signals from the MCPs are directly sensed by the input pads of the bare readout chips. This allows to operate the MCPs at lower gain, with the benefit of increased lifetime. Such devices accommodate high pixel count rate, local data processing and high frame readout speed. The fields of applications include Cherenkov light detection and fluorescence lifetime imaging for which single-photon sensitivity, high time and spatial resolutions are simultaneously required [121].

All of the above demonstrates the potential and evolution of position-sensitive vacuum photon detectors that remain a very active and attractive field.

References

[1] J. Séguinot, T. Ypsilantis, Nucl. Instrum. Methods 142 (1977) 377–391.
[2] The LHCb RICH Collaboration, Eur. Phys. J. C (2013) 73:2431.
[3] S.-O. Flyckt, C. Marmonier (Eds.), Photomultiplier Tubes - Principles and Applications, Photonis, 2002.
[4] Catalogue 'Photomultiplier Tubes', Hamamatsu Photonics K.K., 2016.
[5] E. Nappi, J. Séguinot, Riv. Nuovo Cimento 28 (8–9) (2005).
[6] B.N. Ratcliff, Slac-pub-8989, 2001.
[7] C. Joram, G. Haefeli, B. Leveringtin, J. Instrum. 10 (2015) C08005.
[8] Yu. Musienko, et al., Nucl. Instrum. Methods A 787 (2015) 319–322.
[9] M.G. Bisogni, A. Del Guerra, N. Belcari, Nucl. Instrum. Methods A 926 (2019) 118–128.
[10] C. Jackson, et al., Proc. SPIE 10100, Optical Components and Materials XIV, 101000K (19 April 2017).
[11] The LHCb collaboration The LHCb Detector at the LHC, J. Instrum. 3 (2008) S08005.
[12] A.H. Sommer, Photoemissive Material, John Wiley and Sons, Inc., 1968.
[13] A. Braem, et al., Nucl. Instrum. Methods A 502 (2003) 205–210.
[14] Z. Yusof, et al., Physics Procedia 37 (2012) 733–739.
[15] Hamamatsu Photonics K.K., private communication, 2019.
[16] H. Kume, et al., IEEE Trans. Nucl. Sci. 32 (1) (1985) 355–359.
[17] H. Kume, et al., IEEE Trans. Nucl. Sci. 33 (1) (1986) 359–363.
[18] H. Kyushima, et al., IEEE Trans. Nucl. Sci. 41 (4) (1994) 725–729.
[19] M. Watanabe, et al., IEEE Trans. Nucl. Sci. 44 (3) (1997) 1277–1282.
[20] S. Nagai, et al., IEEE Nuclear Science Symposium Conference Record. (Cat. No. 98CH36255), 1998.
[21] Y. Yoshizawa, et al., IEEE Nuclear Science Symposium Conference Record, 1997.
[22] H. Kyushima, et al., IEEE Nuclear Science Symposium Conference Record, 2000.
[23] Y. Shao, et al., Nucl. Instrum. Methods A 390 (1997) 209–218.
[24] M. Calvi, et al., J. Instrum. 10 (P09021) (2015).
[25] J. Pyrlik, et al., Nucl. Instrum. Methods A 446 (2000) 299–304.
[26] J. Séguinot, et al., Nucl. Instrum. Methods A 297 (1990) 133–147.
[27] J. Pyrlik, et al., Nucl. Instrum. Methods A 414 (1998) 170–181.
[28] P. Krizan, et al., Nucl. Instrum. Methods A 371 (1996) 151–154.
[29] P. Krizan, et al., Nucl. Instrum. Methods A 394 (1997) 27–34.
[30] I. Ariño, et al., Nucl. Instrum. Methods A 516 (2004) 445–461.
[31] E. Albrecht, et al., Nucl. Instrum. Methods A 502 (2003) 112–116.
[32] F. Tessarotto, et al., J. Instrum. 9 (2014) C09011.
[33] M. Contalbrigo, et al., Nucl. Instrum. Methods A 766 (2014) 22–27.
[34] M. Mirazita, et al., Nucl. Instrum. Methods A 952 (2020) 161844.
[35] P. Abbon, et al., Nucl. Instrum. Methods A 587 (2008) 371–387.
[36] J. Agarwala, et al., Nucl. Instrum. Methods A 952 (2020) 161832.
[37] Nikon MicroscopyU web site, Fundamentals of Digital Imaging, https://www.microscopyu.com/digital-imaging/fundamentals-of-digital-imaging.
[38] R.A. Montgomery, et al., Nucl. Instrum. Methods A 790 (2015) 28–41.
[39] S. Blin, et al., IEEE 2010 Nuclear Science Symposium Conference Record.
[40] M. Contalbrigo, et al., Nucl. Instrum. Methods A 952 (2020) 162123.
[41] F. Barbosa, et al., Nucl. Instrum. Methods A 876 (2017) 69–71.
[42] I. Adam, et al., Nucl. Instrum. Methods A 538 (2005) 281–357.
[43] The LHCb collaboration, LHCb PID Upgrade Technical Design Report, CERN-LHCC-2013-022; LHCB-TDR-014.
[44] M. Fiorini, et al., Nucl. Instrum. Methods A 952 (2020) 161688.
[45] E. Albrecht, et al., Nucl. Instrum. Methods A 488 (2002) 110–130.
[46] J. Adamczewski-Musch, et al., Nucl. Instrum. Methods A 952 (2020) 161799.
[47] J. Adamczewski-Musch, et al., Nucl. Instrum. Methods A 876 (2017) 65–68.
[48] C. Pauly, et al., Nucl. Instrum. Methods A 876 (2017) 164–167.
[49] V. Patel, M. Traxler, J. Instrum. 13 (2018) C03038.
[50] I.P. Csorba, Image Tubes, Howard W. Sams & Co. Inc., 1985.
[51] R. Ansorge, et al., Nucl. Instrum. Methods A 265 (1988) 33–49.
[52] J. Alitti, et al., Nucl. Instrum. Methods A 283 (1989) 646–649.
[53] S. Aoki, et al., Nucl. Instrum. Methods A 344 (1994) 143–148.
[54] E. Radicioni, Nuclear Phys. B Proc. Suppl. 85 (2000) 95–100.
[55] C. Angelini, et al., Nucl. Instrum. Methods A 289 (1990) 342–350.
[56] C. Angelini, et al., Nucl. Instrum. Methods A 289 (1990) 356–364.
[57] T. Gys, Nucl. Instrum. Methods A 787 (2015) 254–260.
[58] M. Fouassier, et al., Acta Electron. 20 (1977) 369–378.
[59] L. Castillo Garcìa, et al., Nucl. Instrum. Methods A 787 (2015) 197–202.
[60] I. Adachi, et al., Nucl. Instrum. Methods A 907 (2018) 46–59.
[61] J. Fast, et al., Nucl. Instrum. Methods A 876 (2017) 145–148.
[62] S. Hirose, et al., Nucl. Instrum. Methods A 787 (2015) 293–296.
[63] T. Jinno, et al., Nucl. Instrum. Methods A 629 (2011) 111–117.
[64] D.R. Beaulieu, et al., Nucl. Instrum. Methods A 607 (2009) 81–84.
[65] K. Matsuoka, et al., Nucl. Instrum. Methods A 876 (2017) 93–95.
[66] K. Inami, et al., Nucl. Instrum. Methods A 936 (2019) 556–557.
[67] U. Tamponi, et al., Nucl. Instrum. Methods A 952 (2020) 162208.
[68] Belle II TOP Detector Installation web site, https://www2.kek.jp/ipns/en/post/2016/05/belle2-top-detector-installation.
[69] K. Suzuki, et al., Nucl. Instrum. Methods A 876 (2017) 252–256.
[70] Y. Maeda, et al., Nucl. Instrum. Methods A 952 (2020) 162049.
[71] M. Bessner, et al., Nucl. Instrum. Methods A (2019) http://dx.doi.org/10.1016/j.nima.2019.06.059, in press.
[72] W. Ikegami, Andersson and PANDA collaboration, J. Phys. Conf. Ser. 770 (2016) 012043.
[73] E. Etzelmüller, et al., Nucl. Instrum. Methods A 952 (2020) 161790.
[74] J. Schwiening, et al., J. Instrum. 13 (2018) C03004.
[75] K. Föhl, et al., J. Instrum. 13 (2018) C02002.
[76] A. Lehmann, et al., Nucl. Instrum. Methods A 952 (2020) 161821.
[77] A. Lehmann, et al., Nucl. Instrum. Methods A (2019) http://dx.doi.org/10.1016/j.nima.2019.162357, in press.
[78] M. Düren, et al., Nucl. Instrum. Methods A (2019) http://dx.doi.org/10.1016/j.nima.2019.04.068, in press.
[79] J. Michel, et al., J. Instrum. 12 (2017) C01072.

[80] M.J. Charles, R. Forty, Nucl. Instrum. Methods A 639 (2011) 173–176.
[81] N. Harnew, et al., Nucl. Instrum. Methods A 952 (2020) 161692.
[82] T.M. Conneely, et al., J. Instrum. 10 (2015) C05003.
[83] T. Gys, et al., Nucl. Instrum. Methods A 912 (2018) 53–56.
[84] R. Gao, et al., J. Instrum. 12 (2017) C03008.
[85] N.H. Brook, et al., Nucl. Instrum. Methods A 908 (2018) 256–268.
[86] T.H. Hancock, et al., Nucl. Instrum. Methods A (2019) http://dx.doi.org/10.1016/j.nima.2019.04.014, in press.
[87] T. Gys, Nucl. Instrum. Methods A 595 (2008) 136–141.
[88] N. Sclar, Y.C. Kim, IRE Trans. Electr. Dev. 5 (2) (1958) 110.
[89] R. De Salvo, et al., Nucl. Instrum. Methods A 315 (1992) 375–384.
[90] P. Cushman, et al., Nucl. Instrum. Methods A 504 (2003) 62–69.
[91] M. Moritz, et al., IEEE Trans. Nucl. Sci. 51 (3) (2004) 1060–1066.
[92] P. Weilhammer, et al., Nucl. Instrum. Methods A 384 (1996) 159–166.
[93] A. Braem, et al., Nucl. Instrum. Methods 497 (2003) 202–205.
[94] A. Braem, et al., Nucl. Instrum. Methods A 518 (2004) 574–578.
[95] T. Gys, et al., Nucl. Instrum. Methods A 355 (1995) 386–389.
[96] E. Albrecht, et al., Nucl. Instrum. Methods A 411 (1998) 249–264.
[97] E. Albrecht, et al., Nucl. Instrum. Methods A 442 (2000) 164–170.
[98] K. Wyllie, et al., Nucl. Instrum. Methods A 567 (2006) 184–187.
[99] M. Campbell, et al., IEEE Trans. Nucl. Sci. 53 (4) (2006) 2296–2302.
[100] T. Gys, et al., Nucl. Instrum. Methods A 567 (2006) 176–179.
[101] R. Young, et al., Nucl. Instrum. Methods A 639 (2011) 94–98.
[102] S. Eisenhardt, et al., Nucl. Instrum. Methods A 766 (2014) 217–220.
[103] S. Gambetta, et al., Nucl. Instrum. Methods A 952 (2020) 161882.
[104] R. Pestotnik, et al., Nucl. Instrum. Methods A 876 (2017) 265–268.
[105] Y. Yusa, et al., Nucl. Instrum. Methods A 876 (2017) 149–152.
[106] H. Kakuno, et al., Nucl. Instrum. Methods A 766 (2014) 225–227.
[107] H. Kindo, et al., Nucl. Instrum. Methods A 876 (2017) 269–271.
[108] H. Kindo, et al., Nucl. Instrum. Methods A 952 (2020) 162252.
[109] L. Burmistrov, et al., Nucl. Instrum. Methods A (2019) http://dx.doi.org/10.1016/j.nima.2019.05.073, in press.
[110] T. Szczesniak, et al., IEEE Trans. Nucl. Sci. 61 (5) (2014) 2687–2693.
[111] Catalogue 'micro PMT', Hamamatsu Photonics K.K., 2019.
[112] C. Ertley, et al., Nucl. Instrum. Methods A 912 (2018) 75–77.
[113] A.V. Lyashenko, et al., Nucl. Instrum. Methods A (2019) http://dx.doi.org/10.1016/j.nima.2019.162834, in press.
[114] X. He, et al., Nucl. Instrum. Methods A 952 (2020) 162051.
[115] G. Kalicy, et al., J. Instrum. 13 (2018) C04018.
[116] Y. Ileva, et al., J. Instrum. 13 (2018) C03018.
[117] L.M. Hirvonen, et al., Nucl. Instrum. Methods A 787 (2015) 323–327.
[118] T. Cajgfinger, et al., Nucl. Instrum. Methods A 787 (2015) 176–181.
[119] J. Vallerga, et al., J. Instrum. 9 (2014) C05055.
[120] A.S. Tremsin, et al., Nucl. Instrum. Methods A 787 (2015) 20–25.
[121] M. Fiorini, et al., J. Instrum. 13 (2018) C12005.